Macromolecules

pubs.acs.org/Macromolecules Article

Nonlinear Shear Rheology of Unentangled Polymer Melts

Maxime Dalne, Salvatore Costanzo, Katerina Peponaki, Nuofei Jiang, Stelios Alexandris, Nino Grizzuti, Dimitris Vlassopoulos,* Michael Rubinstein,* and Evelyne van Ruymbeke*

Cite This: *Macromolecules* 2025, 58, 7062−7083 Read Online

ACCESS | Metrics & More | Article Recommendations | Supporting Information

ABSTRACT: In the present work, we investigate the nonlinear shear rheology of unentangled polymer melts. We use linear polystyrenes with molar mass of 10, 20, or 30 kg/mol. The measurements of shear and normal stress are performed using cone-and-partitioned-plate rheometry. While the linear viscoelastic response is consistent with predictions of the Rouse model, in the nonlinear regime, the Cox−Merz rule is not fully validated, despite a universal thinning exponent of −0.5. These experimental results are analyzed using the recent shear slit model of Parisi et al. and molecular dynamics simulations. A new molecular picture is proposed to explain the origin of the transient stress overshoot, based on the concept of the advection time that marks the transition between affine and nonaffine deformation. Finally, a simple model is developed, by combining Rouse relaxation modes, chain confinement to shear slit in the velocity gradient direction and tension blobs in the velocity direction. The predictions of this model for shear viscosity are in excellent agreement with the experimental data and consistent with simulations.

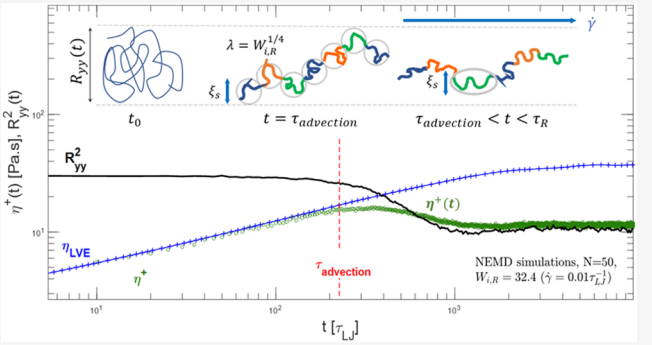

I. INTRODUCTION

The linear viscoelastic properties of unentangled and entangled polymer melts and solutions are rather well understood.[1−8] Different models have been proposed to predict their behavior on the quantitative level, including the Rouse model for unentangled polymers,[2] the tube,[1,9] or slip-link[10−12] models for entangled polymers. In contrast, the understanding of polymer dynamics under nonlinear deformations has not reached the same level of success, despite its crucial importance in controlling the processing of polymeric materials. Hence, many fundamental questions need to be addressed to achieve a satisfactory description of nonlinear viscoelastic response upon fast shear,[13−18] or elongation deformations.[19−24]

In the present work, we focus on the viscoelastic response of unentangled polymer melts during start-up shear flow at a constant shear rate $\dot{\gamma}$. A very limited amount of data is available in the literature and has recently motivated a significant activity in modeling with the aim of understanding the molecular mechanisms at work, as briefly outlined below. The early work of Stratton[25] provided steady shear viscosities as a function of the shear rate for PS melts with molar masses of 10.5 and 19.8 kg/mol. The experiments were performed with capillary rheometry and yielded the apparent steady shear viscosity with a thinning exponent of about −0.5. Later, Santangelo and Roland[26] performed start-up shear measurements of PS melts with a molar mass 13.7 kg/mol in a rotational rheometer. To minimize the compliance effects of the transducer near the glassy regime, the authors used parallel plates and corrected for the nonconstant shear rate. They also reported the first normal stress coefficient, though normally this geometry gives access to the difference between the first and second normal stress differences. The maximum Weissenberg number attained was about 5. The authors also found a shear-thinning exponent of −0.5. Under these experimental conditions, no edge fracture was reported. Overall, these two data sets are very useful and have served as a reference to assess different models. However, it is necessary to obtain more data, with different molar masses, using more suitable experimental setups to circumvent experimental issues such as wall slip and edge fracture instability. In this respect, a cone-partitioned plate (CPP) fixture seems to be appropriate.[27−29] Therefore, in this work, our first objective is to further investigate experimentally the nonlinear shear response of unentangled PS melts, to gain more insight about their properties.

In addition to the experimental data, there is a need to perform nonequilibrium molecular dynamics (NEMD) simulations[30−34] in order to further understand the evolution of the chains' conformation under constant shear rate. We have recently addressed the role of chain stiffness and monomeric

Received: February 27, 2025
Revised: June 21, 2025
Accepted: June 30, 2025
Published: July 8, 2025

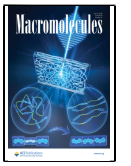

https://doi.org/10.1021/acs.macromol.5c00553
Macromolecules 2025, 58, 7062−7083

friction in unentangled melts.[35] Both the experimental and simulation results are then used to propose a molecular picture to explain the transient response and the shear thinning properties of these samples that are consistent with modeling.[35−37]

Regarding modeling, we aim to investigate and model the shear thinning viscosity and normal stress coefficients, which have been observed in both experiments[26,38−41] and simulations,[30−34] at shear rates larger than the inverse Rouse time of the entire chain, $\dot{\gamma} > \frac{1}{\tau_R}$. In the linear regime of deformation, the motions of unentangled chains are not constrained by the surrounding chains, and the stress relaxation is described by the Rouse model.[1,2] The corresponding stress relaxation modulus can be approximated by

$$G_{R,\mathrm{LVE}}(t) = \frac{\rho RT}{M} \sum_{p=1}^{N} \exp\left(-\frac{2p^2 t}{\tau_R}\right) \tag{1}$$

where N is the number of Kuhn segments in the chain, ρ is the density, M is the molar mass of the chains, R is the ideal gas constant, and T is the absolute temperature. Despite the fact that some studies and molecular simulations (such as Kremer−Grest bead−spring simulation,[42,43] dissipative particle dynamics simulations,[44,45] full-atomistic molecular dynamics simulations[45,46]) have demonstrated that the local chain dynamics is not fully consistent with Rouse predictions,[45] this model is able to provide a simple and accurate description of the relaxation of the unentangled polymer in the linear regime. However, in the nonlinear regime, it is unable to account for the observed shear thinning as it predicts that the chains stretch along the flow direction but are unperturbed in the directions orthogonal to the flow.[40,41]

To explain the shear thinning of the material functions, several approaches have been proposed in the literature. Recently, Ianniruberto and Marrucci[13,19] introduced the concept of friction reduction in order to model the thinning properties observed in both shear and elongational flow of polymer melts. The decrease of the monomeric friction coefficient is attributed to the alignment of the Kuhn segments with the flow. Hence, this mechanism mainly affects the long chains and should be predominant for polymer melts. This concept has been successfully implemented for both entangled PS melts and solutions under elongation flow.[19] It has also been applied to explain the experimentally observed shear thinning of the unentangled polystyrene melts mentioned above,[25,26] using a model based on Fraenkel chains containing an appropriate number of links (which represent the Kuhn segments of the polymer) and performing Brownian dynamics simulations.[13] This approach was validated by comparing the theoretical predictions to the transient experimental data (both shear and normal stress growth coefficients). Unexpectedly, even at relatively low Weissenberg numbers (Wi_R), friction reduction was necessary in order to describe the experimental data. However, as mentioned by the authors, the limited available nonlinear shear data of unentangled melts do not allow for a full assessment of the role of flow-induced reduction of the monomeric friction coefficient. Furthermore, it remains difficult to predict the friction coefficient, only based on the shear flow data and the sample's characteristics.

Using the friction reduction concept, Watanabe et al.[47] analyzed the dynamics of unentangled Rouse chains under fast flow, while accounting for possible changes in the segmental friction coefficient, but also in the intensity of the Brownian force between the test chain and its surrounding. By solving the Langevin equation of the Rouse model, the authors derived analytical expressions for the nonlinear rheological properties and the end-to-end stretch ratio under steady shear and extension. They showed that it is possible to reach a quantitative description of the shear thinning viscosity of PS (the data of Santangelo and Roland[26]) as well as their viscoelastic response under elongation, and in particular for the new experimental data of a PS melt with weight-average molar mass M_w = 27 kg/mol and poly(*p*-*tert*-butylstyrene) PtBS, melt with M_w = 53 kg/mol.[22] This required, however, the accurate determination of the ratio between the nonequilibrium parameters related to the friction and the Brownian force intensity.

An alternative approach for modeling the nonlinear rheology of unentangled polymers, which does not rely on the hypothesis of friction coefficient reduction, was recently developed by Wagner and co-workers.[48−50] It is a single integral constitutive equation based on a Rouse-type relaxation modulus, which considers the orientation and stretch of many independent polymer strands, each representing a different relaxation mode of Rouse chains. This approach was successfully tested in elongation and under shear by quantitatively describing the data of Stratton[25] and Santangelo and Roland.[26] However, to achieve this, it was necessary to impose a restriction that the different strands cannot stretch more than an amount defined by a finite conformational stretch parameter.

A simple scaling approach has been proposed by Colby and co-workers,[40] based on the Rouse model and on the concept of tension blobs.[51] A tension blob represents the largest length scale above which chain sections are stretched by the shear stress and depends on the imposed shear rate.[41] According to this approach, in a steady state, the sheared polymer chains can be seen as a linear array of tension blobs, and the authors assume that the chain size in the velocity gradient direction is the size of one tension blob. The Rouse relaxation modes are active on the portions of the chain that are not stretched and can relax and dissipate energy, i.e., inside the blobs, while the longer modes, corresponding to subchains larger than the tension blobs, are too slow to relax. Consequently, their reduced dissipation results in a lower apparent viscosity at high shear rates, scaling with a power law $\eta \sim \dot{\gamma}^{-1/2}$ in the thinning regime, in agreement with both experimental and simulation results.[41,52] Therefore, this concept, which has also been recently implemented in the time marching algorithm (TMA) tube model[53−55] to predict the steady shear viscosity of entangled polymer melts, represents an appealing starting point to interpret the shear properties of unentangled polymers, even though the proposed equations do not allow to describe the elastic effects, such as normal stresses.

The latter point has been addressed by Parisi and co-workers,[41] who recently developed a "shear slit" model to explain the variation of the steady-state shear viscosity with the Weissenberg number of entangled ring polymer melts. Their model includes two different length scales: First, the size of the shear strands (called shear blobs in the paper) in the velocity gradient direction. It is independent of the molar mass of the chains and refers to the longest subchains that can relax during a time period equal to the inverse shear rate, $\tau_s = \tau_{\mathrm{rel}}(M_s) = 1/\dot{\gamma}$, where M_s is the molar mass of a shear strand.

https://doi.org/10.1021/acs.macromol.5c00553
Macromolecules 2025, 58, 7062−7083

These shear strands represent the confinement effect induced by the nonlinear shear flow on the polymer chains, as the latter can only equilibrate at length scales shorter than these sections. Consequently, the relaxation modes in the direction of the velocity gradient are self-consistently constrained to within the scale of the shear slits, the size of which decreases with the shear rate. The second length scale is the size of the tension blob, defined in the velocity direction. This length scale determines the level at which the chains are stretched in this direction. Since the stretch can be important, especially for long chains, the tension blob size is smaller than the shear strand size. Furthermore, it depends on the molar mass of the chains. Based on this model, the authors could correctly reproduce the scaling laws obtained by simulations and experiments of sheared melts of noncatenated cyclic polymers. As in ref 40,41, in the nonlinear regime, the observed shear thinning is a consequence of the fact that the dissipation is only due to thermally equilibrated modes of the chain on length scales up to the shear strand. However, an important advantage of considering both shear strands and tension blobs is that the model is capable of reproducing both the stretch of the chain and the first and second normal stress differences, which is not the case if only the tension blobs (or only shear strands) are considered.

Thus, the current works adopt essentially two ways to model the nonlinear shear properties of unentangled polymers and explain their shear thinning. It is taken into account either through the flow-induced reduction of the monomeric friction or by considering that the relaxation modes slower than the flow do not contribute to the steady-shear viscosity.[40] These two approaches are a priori not contradictory, as they both consider that under high shear in the steady regime, the drag force exerted on the chain is reduced compared to the linear regime. Their main difference probably lies in the influence of the molecular environment on the motion and stretch of a specific chain. To further validate these different models, new experimental data as well as new simulation data are required.

The objective of the present work is to further investigate the nonlinear shear properties of unentangled linear polymers, both experimentally and theoretically, in order to develop a consistent universal picture for the shear viscosity. To this end, we measured and analyzed the transient shear data of several unentangled polymer melts using a custom-made CPP geometry. The data were measured in a relatively wide range of shear rates. Specific points are discussed, such as the influence of the glassy relaxation modes on the transient shear data and the validity of the time−temperature superposition (TTS) principle in the nonlinear regime. Indeed, the regime of interest involves shear rates that correspond to the intermediate frequency range, i.e., before the chains reach their terminal relaxation regime but shortly after the relaxation of their glassy modes. However, with short chains, the latter transition is not well-defined. These experimental data are analyzed and discussed together with nonequilibrium molecular dynamics (NEMD) simulations of unentangled melts,[35] and a molecular picture to explain the transient shear data is proposed. Following ideas based on and extending the shear slit model,[41] we develop a simple model to predict the transient and steady viscoelastic behavior of these polymers. We show that, despite being semiphenomenological, the model predicts both the transient and steady viscoelastic data with no additional parameters compared to the linear regime. Note that a summary of the different parameters used in the model is given in (SI Table 1).

The organization of the paper is the following: we first present, in Section II, the samples used in this work along with the experimental techniques. Then, in Section III, the experimental results are presented and discussed, first in the linear regime (Section III.I) and then in the nonlinear regime, together with simulation data (Section III.II). The new model is then presented and compared with the experimental data on viscosity and normal stresses. Finally, conclusions are drawn in Section IV.

II. MATERIALS AND METHODS

II.I. Materials. Three nearly monodisperse unentangled polystyrene (PS) samples with molar masses M_w of about 10, 20, and 30 kg/mol, were purchased from Polymer Source and Agilent Technologies and used without any further purification. Their molecular characteristics (glass transition temperature T_g, monomeric time τ_0, and terminal Rouse time τ_R) are listed in Table 1. The polydispersity of all samples was reported to be 1.02.

Table 1. Molecular Characteristics of the Polystyrene Samples

samples	M_w [kg/mol][a]	T_g [°C]	τ_0 (T) [ms (°C)]	τ_R (T) [s(°C)]
PS10k	10.5	96.1	4.2 (115)	0.844 (115)
PS20k	19.3	101.5	1.4 (125)	1.12 (125)
PS30k	29.1	102.7	0.71 (130)	1.3 (130)
PS30k	29.1	102.7	2.3 (125)	4.2 (125)

[a]Weight-average molar mass measured by Static Light Scattering (information provided by Agilent).

II.II. Rheological Measurements. To perform rheological measurements, the samples were shaped into discoid specimens using vacuum compression molding.[56] Care was needed when extracting them from the mold due to their brittleness and the large diameter/thickness ratio. In some cases, the powders were cold-pressed to discoid tablets and melted directly onto the rheometer. A very good agreement was found between data on samples prepared with the two different protocols.

Rheological measurements were performed on two different ARES strain-controlled rheometers (TA, USA) equipped with force rebalance transducers (2KFRTN1) and a double-head MCR702 (Anton Paar, Austria) operating in strain-controlled mode, in two laboratories (Naples and Crete), as explained below. Nitrogen convection ovens were used for temperature control and for creating an inert atmosphere. A good agreement was observed between the different sets of data. As far as the oscillatory data are concerned, the standard deviation of the measurements in the two laboratories was such that error bars are within the size of the symbols in Figure 1. Concerning start-up shear tests, at a fixed shear rate, variations of the shear stress growth coefficient (also called transient viscosity) curves, $\eta^+(t) = \sigma^+(t)/\dot{\gamma}$, collected in the two laboratories were of the order of ±10%. The reproducibility of the transient data in the same laboratory also shows a variation of 10%. Characteristic error bars are added to the last transient data point in Figure 5 to provide an idea of the experimental uncertainty.

The linear viscoelastic data were measured with stainless steel parallel plate geometry (8 mm diameter for ARES and 4 mm diameter for MCR702), and effects of transducer compliance were accounted for using the correction procedure reported in literature[57,58] (see also Section III below). The nonlinear rheometry was performed on the ARES rheometers with the stainless steel CPP geometries, and details can be found in ref 29. In brief, the bottom fixture is a standard cone with a diameter of 25 mm, a cone angle of 0.1 rad, and a truncation of 53 μm. The upper fixture consists of an inner measuring plate and an outer nonmeasuring ring attached to the head of the transducer. The

https://doi.org/10.1021/acs.macromol.5c00553
Macromolecules 2025, 58, 7062−7083

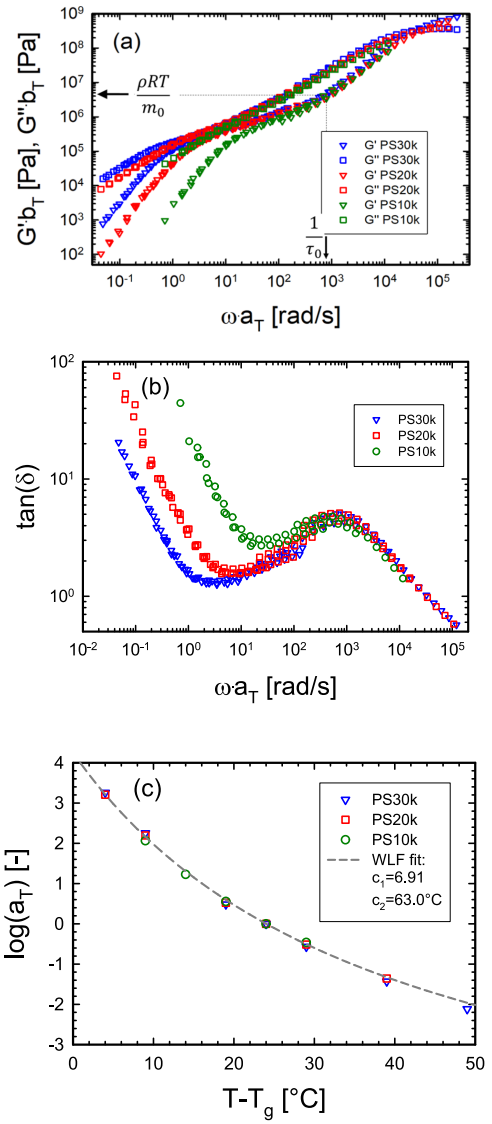

Figure 1. (a) Linear viscoelastic master curves at the same distance from the glass transition temperature ($T_{ref} = T_g + 24$ °C). The arrow indicates the value of $\frac{\rho RT}{m_0}$, with $m_0 = 720$ g/mol, the molar mass of a Kuhn segment; (b) respective tanδ curves of the same PS melts; (c) shift factors used to construct the master curves of panels (a, b). The high-frequency data were checked for transducer compliance effects.

geometry is modular, so an inner plate with a radius R_i of either 3 mm or 5 mm was mounted. The outer ring was also adjusted accordingly. The gap between the inner plate and the outer partition is ≤100 μm. The role of the outer ring is to house a sample with a larger radius $R_e > R_i$. Using a sample with a radius larger than R_i ensures a reliable torque signal but may affect the normal stress signal if a fracture occurs. This is discussed in detail in ref 59 but it is not further considered here because only signals reaching a true steady state were accounted for in extracting the normal stress differences. Hence, the first normal stress difference obtained from the axial force signal is an apparent one, $N_{1,app}$, and involves the contribution of both real first and second normal stress differences (N_1 and N_2, respectively), such as $N_{1,app} = N_1 + 2(N_1 + 2N_2)\ln\left(\frac{R_e}{R_i}\right)$. This suggests that, if two independent points of the linear function $N_{1,app} = f\left(\ln\left(\frac{R_e}{R_i}\right)\right)$ are available, N_1 and N_2 can be determined.

III. RESULTS AND DISCUSSION

III.I. Linear Viscoelasticity. *III.I.I. Experimental Data.* Figure 1a reports the linear viscoelastic spectra of the polystyrene samples at the same distance from the glass transition temperature ($T_{ref} = T_g + 24$ °C), while Figure 1b reports the corresponding loss factor (tan δ) curves. At high frequencies, the viscoelastic spectra overlap. This region corresponds to the glassy relaxation, which is expected to be the same for the different samples, as it involves monomeric length scales. At intermediate frequencies, the data do not behave as described by the Rouse model, i.e., with both viscoelastic moduli overlaying on a power law with an exponent of 0.5. This is attributed to the fact that the glassy relaxation modes are coupled to the Rouse modes of the spectrum, as can be seen in Figure 1a which shows the relaxation time τ_0 of a Kuhn segment and its corresponding modulus $\rho RT/m_0$, with the molar mass of a Kuhn segment m_0 = 720 g/mol. At low frequencies, the sample reaches its terminal relaxation. The latter is characterized by lower values of the viscoelastic moduli with increasing molar mass, as expected since the Rouse modulus is reciprocally proportional to the molar mass, $G_R = \rho RT/M$.

The master curves were built by horizontally shifting the loss factor data, and the shift factors were subsequently determined. From Figure 1b, one can see that a slight failure of the time−temperature superposition occurs in the intermediate regime, especially for the sample PS10k. Such a failure of TTS in the glass-to-rubbery transition zone has been already observed by other authors.[58,60−62] Nevertheless, as shown in Figure 1c, for the three samples, a William−Landel−Ferry (WLF) dependence of the horizontal shift factors on temperature was observed.[63] All shift factors collapse onto a single curve when compared at the same distance from the glass transition.[64] The extracted WLF constants are C_1 = 6.91 and C_2 = 63 K at a reference temperature of $T_{ref} = 124$ °C + ΔT_g (with $\Delta T_g = T_g - 101.5$ °C). It must be noted that, in order to obtain such a good superposition of the shift factors, we had to consider slightly different values of T_g for samples PS10k (95.5 °C in place of 96.1 °C) and PS30k (101.5 °C in place of 102.7 °C), compared to the measured ones. This difference stays within the acceptable experimental error. Vertical shift factors were also used to account for the variation of (ρT) with temperature, following ref 65. For the experimental temperature range, it was found that the values of the vertical shift factors are within the range 0.95−1.04, therefore they are not reported here.

The failure of TTS observed in Figure 1a,b, in the transition regime between glassy and Rouse modes, is further highlighted in Figure 2. It depicts the shear stress growth coefficient $\eta^+(t)$ of PS30k, obtained in the linear regime (at shear rates corresponding to $Wi_R \ll 1$) at three different temperatures, namely 120, 125, and 130 °C, and shifted to the reference temperature of 130 °C using the shift factors of Figure 1c. It is observed that these data in the linear regime (that we call LVE envelope, $\eta_{LVE}(t)$) superimpose at long times, close to their steady viscosity. However, this is not the case at short times in the glassy regime. As further discussed in Section III.II.IV below, this may affect the steady viscosity of the samples deformed at a very high shear rate. Therefore, both the linear and nonlinear data were modeled at each temperature, separately, to avoid any uncertainties coming from these shift factors.

https://doi.org/10.1021/acs.macromol.5c00553
Macromolecules 2025, 58, 7062−7083

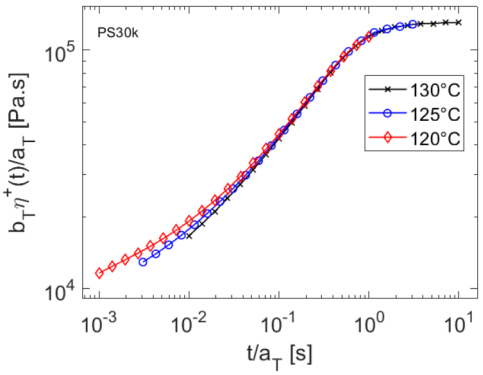

Figure 2. Comparison of the stress growth coefficient of PS30k in the linear regime (low shear rates), measured at different temperatures (120, 125, and 130 °C), and shifted to the reference temperature of 130 °C. This is the LVE envelope, $\eta_{LVE}(t) = b_T\eta(t)^+|_{lowrate}/a_T$.

III.I.II. Modeling. As already mentioned, the relaxation of unentangled PS chains containing N Kuhn segments is well approximated in the linear regime by the Rouse relaxation (eq 1). According to this model,[2] each relaxation mode p, with $1 \leq p \leq N$, corresponds to the relaxation of subchains containing N/p Kuhn segments with relaxation time $\tau_p \approx \frac{\tau_R}{p^2}$ (eq 1). Thus, at the time τ_p, as illustrated in Figure 3, the chain can be represented by a series of equilibrated chain sections of size $b\sqrt{\frac{N}{p}}$ (with b, the length of a Kuhn segment).

After a step strain, the chain is partially oriented, and each Kuhn segment contributes to the modulus $G(t)$. The chain renews its configuration (loses its orientation) with time, first at the level of the Kuhn segments, then at the level of larger and larger chain sections. This leads to a decrease of $G(t)$, which is proportional to the number density of these unrelaxed chain sections (containing $\frac{N}{p}$ Kuhn segments at time τ_p). The Rouse relaxation process takes place until the relaxation of the entire chain occurs, at time $t = \tau_R$. The latter is defined as $\tau_R = \tau_0 N^2$. The values of τ_0, which vary with both the molar mass of the samples and temperature, have been fixed by best-fitting procedure, and are given in Table 1. As shown in the SI (see Figure S1), they are slightly different from their theoretical value, $\tau_0(T_{ref}) \times a_T$ determined based on the WLF Equation at iso-T_g condition. However, the variation found between the best-fitting and the theoretical values corresponds to a maximum of 1 °C of uncertainty at the given measurement temperature. Note that the value of ρRT in eq 1 has been taken to be 3.4×10^9 Pa g/mol, consistent with our previous works with PS samples.[15] Polydispersity is taken into account by assuming that the molar mass distribution is well represented by a log-normal function. More details on the implementation of this method and its influence on the viscoelastic data are given in SI (Figure S2).

The comparison between model predictions and experimental data is shown in Figure 4, which depicts the storage (G') and loss (G'') moduli of PS20k measured at 125 °C and PS30k measured at 125 and 130 °C. Respective predictions of eq 1 lead to an excellent description of the experimental data in the low-frequency regime. As mentioned, however, at high frequencies, the glassy modes have a large influence on the data, which cannot be accounted for by the Rouse model, according to which both G' and G'' superimpose and have a slope of 0.5. As shown in ref 66, the contribution of these glassy modes to the relaxation modulus can be described by

$$G_{glassy}(t) = G_\infty\left[1 - \mathrm{erf}\left(\sqrt{\frac{t}{\tau_0}}\right)\right] \quad (2)$$

This extra segmental relaxation process must be added to the Rouse expression (eq 1), such that the relaxation modulus becomes $G(t) = G_R(t) + G_{glassy}(t)$. In eq 2, G_∞ is the glassy modulus. With this addition, the LVE are well-described throughout the entire frequency spectrum (see the dashed curves in Figure 4), even though the simple addition of the glassy and Rouse modes to describe the relaxation modulus is, a priori, not valid and should be considered as an approximation.[67,68] It is also noted that the LVE response of PS30k at 130 °C is in good agreement with the Rouse model, suggesting that this sample can be considered unentangled.

III.II. Nonlinear Viscoelasticity. *III.II.I. Experimental Data.* Figure 5 shows the shear stress growth coefficients of the unentangled PS melts measured at different temperatures. The reported LVE envelopes are obtained from a multimode Maxwell fit of the experimental master curves presented in Figure 1a.

As represented in Figure 4 (see the star symbols), the measuring temperatures of the transient data were selected in a way to span shear rates from the LVE regime to well within the nonlinear regime, while avoiding the intervention of glassy modes as much as possible. From Figure 5, at times shorter than 0.05−0.07 s (depending on the sample and temperature measured), the LVE envelope does not agree well with the transient shear data. The mismatch is due to multiple reasons:

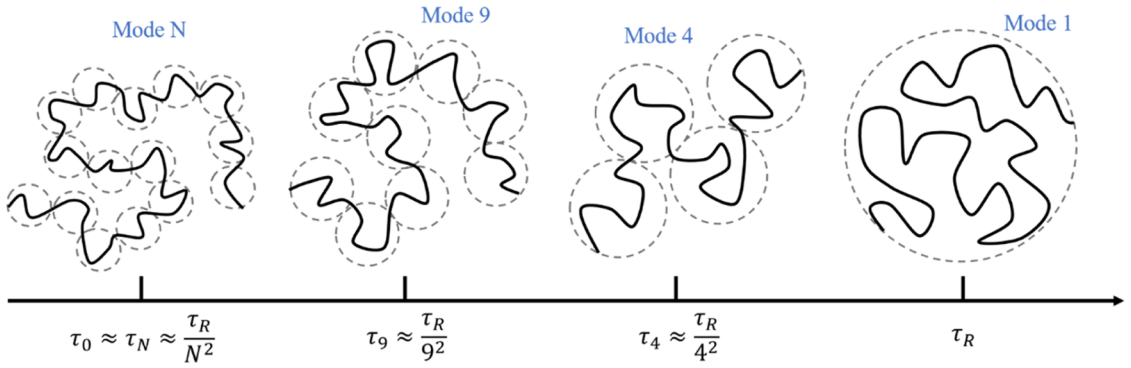

Figure 3. Rouse relaxation of an unentangled linear chain in the linear regime. Each Rouse chain section has a root-mean-square size $b\sqrt{\frac{N}{p}}$.

https://doi.org/10.1021/acs.macromol.5c00553
Macromolecules 2025, 58, 7062−7083

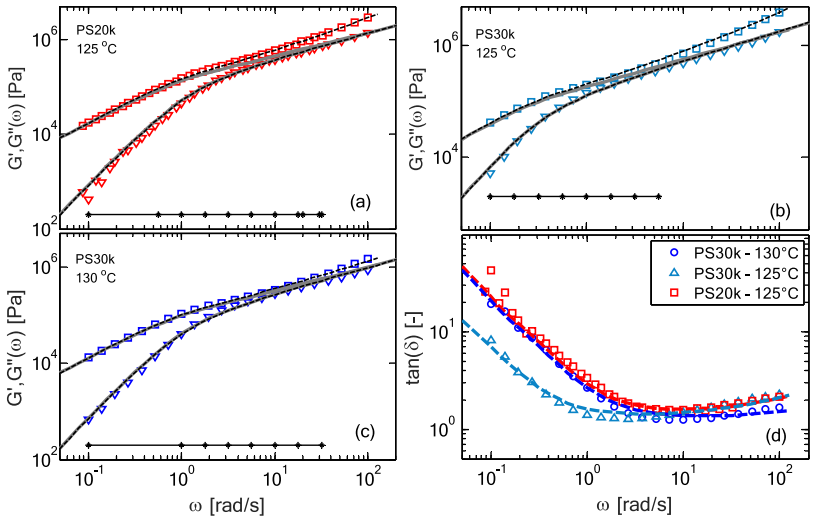

Figure 4. Experimental storage (▽) and loss (□) moduli of PS20k at 125 °C (a) and PS30k at 125 °C (b) and 130 °C (c), and the respective loss tangent? (d), as a function of angular frequency. Predictions with and without glassy modes are depicted by dashed and solid curves, respectively. The black lines with star symbols indicate the frequencies corresponding to the shear rates at which the nonlinear shear responses have been measured.

one is the finite response time of the motor to reach the constant angular velocity set for start-up experiments, which is of the order of 0.1 s. Therefore, transient shear data at times earlier than 0.1 s are not fully reliable. Another source of error is the multimode Maxwell fitting of the master curves of Figure 1a, as the region from 10^{-2} to 10^{-1} s corresponds to time scales where the linear oscillatory data start being affected by thermorheological complexity (due to the glassy modes). Moreover, the data at high shear rates are limited by transducer resonance and edge fracture (this was mitigated by employing CPP).[26] Whereas the transducer resonance issue at lower temperatures was already reported in the literature[26,57,58] and was also observed here and mitigated by using small diameter plates, edge fracture was not addressed before, apparently because of the low Weissenberg number attained.[26]

The transient response of the unentangled PS in Figure 5 is qualitatively similar to that of entangled PS melts.[15] As the Weissenberg number exceeds unity, an overshoot in the transient signal appears before the steady state is attained, and the steady-state viscosity undergoes shear thinning. At higher rates, we found that the overshoot is more pronounced and that an undershoot also appears, akin to entangled melts (see SI, Figure S3). In spite of the analogy with entangled PS melts,[15] the analysis of the nonlinear data of unentangled melts reveals some striking differences. First of all, when the steady-state viscosity is plotted as a function of the Weissenberg number (see Figure 6a), we observe a shear thinning exponent of −0.5 for unentangled melts and the normalized curves of the different unentangled samples superimpose onto a universal curve, while the shear thinning exponent varies from −0.8 for moderately entangled to −0.9 for well entangled polymers.[15,41] This is in agreement with the experimental data reported in refs 26,40,41, as well as with the simulation results for unentangled polymers.[45,46] However, as further discussed in Section III.II.III, the fact that the thinning exponent is −0.5 does not imply that the Cox−Merz rule[69] is fully satisfied.

It is also observed that the ratio of the maximum transient to the steady-state viscosity, $\eta^+_{max}/\eta_{steady}$ has a weaker dependence on the Weissenberg number for unentangled polymers in comparison to their entangled counterparts (see Figure 6b). In particular, for $Wi_R > 1$, the power-law dependence of this ratio has an exponent of about 0.1, which is lower than the exponent of ∼0.2 for entangled polymers.[18,27,28,70,71] Moreover, Figure 6c shows that for $Wi_R > 1$, the slope of $\gamma_{max}(Wi_R)$ progressively decreases when the molar mass of the unentangled samples decreases. This change of slope must be considered with care as it is largely influenced by the contribution of the glassy modes, as further discussed in Section III.II.IV.II. The slope of $\gamma_{max}(Wi_R)$ for PS10k is close to zero, and the value of $\gamma_{max}(Wi_R)$ is around 2.3. It must be noted that, since the chains are unentangled, the value of $\gamma_{max} = 2.3$, which is close to the prediction for entangled polymers,[1] cannot be attributed to the value found for oriented entangled chains sheared at $Wi_R \leq 1$.

As mentioned above, the CPP geometry also allows obtaining the first and second normal stress differences as a function of the flow strength if the apparent normal stress signal is probed for different values of sample radii. This can be achieved either by running multiple measurements with a single CPP on samples of different outer radii[72] or by using a modular CPP fixture having two different inner diameters.[29] We extracted the first and second normal stress differences for PS20k and PS30k from measurements performed in both Naples and Crete. In Naples, the protocol of ref 72 was adopted, whereas in Crete that of ref 29. The axial compliance[73] was considered, and the associated axial response time was lower than the time to reach a steady state (see SI, Figure S4). The analysis was limited to the steady-state values. Moreover, only the data at lower Wi_R are reported, to minimize the influence of outer edge distortion on the normal stress signal.[59] Figure 7a,b show the N_1 and N_2 data for the two PS samples, PS20k and PS30k. They reflect a collection of several measurements from both laboratories (see also Figures S4 and S5). We note that these types of measurements are very sensitive to experimental conditions, as the distortion of the sample's outer edge and the quality of the transient apparent normal force signal can strongly influence the value of N_2. However, the fact that the data from the two laboratories are in good agreement and reproducible (Figure S4) provides confidence about the reliability of the measurements. The above issues prohibited obtaining reliable data for PS10k. In

https://doi.org/10.1021/acs.macromol.5c00553
Macromolecules 2025, 58, 7062−7083

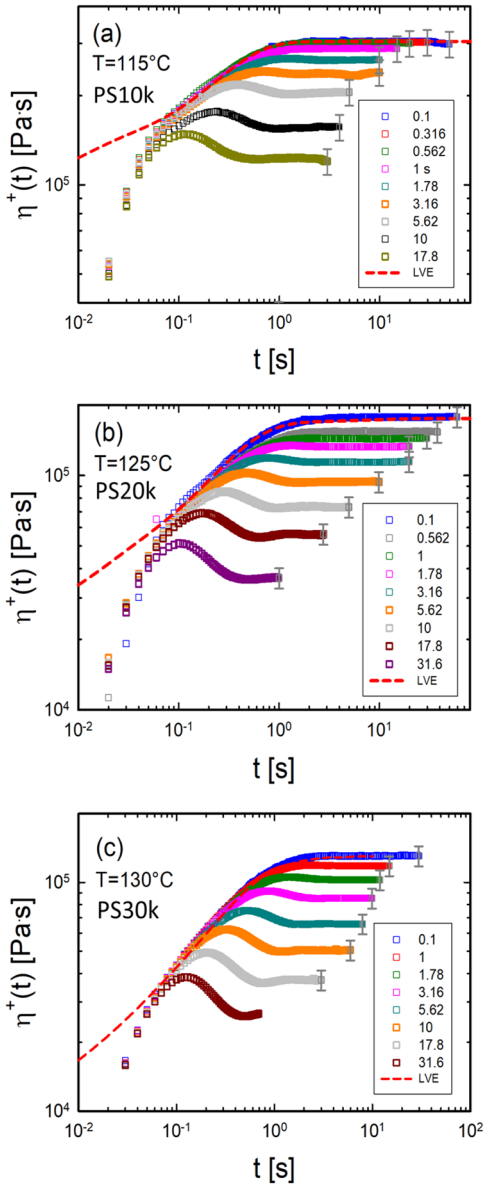

Figure 5. Shear stress growth coefficients vs time for (a) PS10k; (b) PS20k; (c) PS30k, at different temperatures and imposed shear rates, as indicated in the legends.

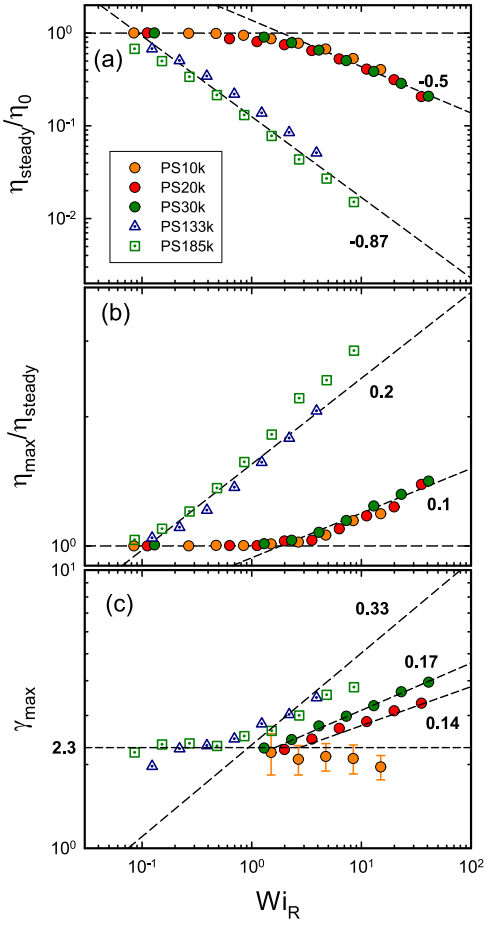

Figure 6. Normalized steady viscosity (a), the ratio of maximum to steady-state viscosity (b), and strain at the overshoot (maximum) transient viscosity (c), as a function of the Weissenberg number Wi_R for the three unentangled PS investigated (filled symbols). For comparison, the data obtained with two well-entangled and nearly monodisperse PS (with molar masses 133 and 185 kg/mol; see reference 15 for their characterization) are also presented (open symbols).

Figure 7c, we demonstrate a very good agreement of the data with the empirical rule of Laun,[74] according to which the first normal stress coefficient in the steady-state regime can be approximated by

$$\Psi_{1,\text{steady}} \equiv \frac{N_1}{\dot{\gamma}^2} \approx \left.\frac{2G'(\omega)}{\omega^2}\right|_{\omega=\dot{\gamma}} \tag{3}$$

This gives additional confidence in the quality of the normal stress data.

The main outcome of the nonlinear transient data is that N_2 is negative and non-negligible in the range of shear rates explored. Furthermore, it emerges that the ratio $-N_2/N_1$ is weakly shear thinning (see SI, Figure S6).

III.II.II. Simulation Results. The transient shear properties of the unentangled polymer melts were also investigated with Non-Equilibrium Molecular Dynamics (NEMD) simulations. We considered a melt of Kremer−Grest chains, the nonlinear rheological properties of which have been recently analyzed from a different perspective[35] (see Section III.II.III.III). The essential details on the simulation method can be found in that work, and are briefly summarized in the SI. In the present work, we simulate melts with either 50 or 100 monomers in each chain and 400 chains in the simulation box. These systems, named N50 and N100, respectively, are in the unentangled regime as the number of monomers in an entanglement strand is around 65 based on the primitive path analysis (PPA).[75] The unentangled state of the chains as well as the good description of their storage and loss moduli have been verified and are shown in the SI (see Figure S5).

Figure 8 presents the main results obtained in the transient and steady-state regimes for N50, at shear rates $\dot{\gamma}$ = 0.001, 0.003, 0.01and 0.03 τ_{LJ}^{-1}, where τ_{LJ} is the Lennard−Jones time (see SI). The Rouse time of the N50 melt has been determined from the Rouse mode analysis as $\tau_R \cong 3240\tau_{LJ}$ (see also SI, Figure S7) and these shear rates correspond to Wi_R = 3.24, 10, 32.4, and 100. The different components of the mean-square end-to-end distance tensor, i.e., $R_{xx}^2(t)$ in the flow direction, $R_{yy}^2(t)$ in the velocity gradient direction, and the $R_{zz}^2(t)$ in the vorticity direction are depicted in Figure 8a, while the

https://doi.org/10.1021/acs.macromol.5c00553
Macromolecules 2025, 58, 7062−7083

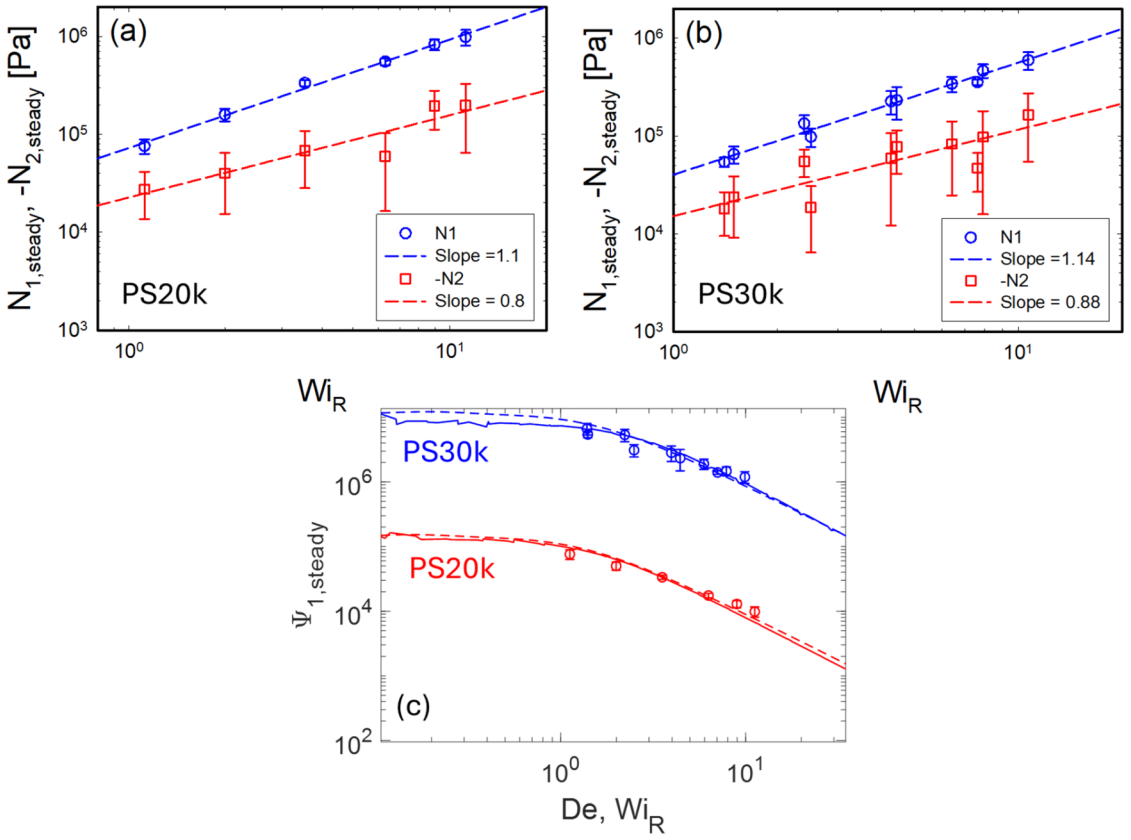

Figure 7. Steady-state first and second normal stress differences as a function of the Weissenberg number for PS20k at 125 °C (a) and PS30k at 130 °C (b). (c) Comparison between the steady-state first normal stress coefficient $\Psi_{1,steady}$ (symbols) and its approximation, based on the rule of Laun[74] (eq 3) and considering the storage modulus either from the experimental data (continuous curves) or from the Rouse model (dashed curves, obtained from eqs 1 and 2).

corresponding shear stress growth coefficient is presented in Figure 8b. Several interesting features can be highlighted: First, we observe a gradual decrease of $R^2_{yy}(t)$ with time, which suggests the gradual confinement of the chains, as invoked in the shear slit model. This process starts at a time that we call $\tau_{advection}$, which corresponds to the time when the end-to-end vector stops deforming affinely and which is further discussed in Section III.II.IV. It must be noted that in Figure 8 and the following figures, the value of $\tau_{advection}$ has been determined theoretically (see Section III.II.IV). The advection time also corresponds to the time at which the shear stress growth coefficient $\eta^+(t)$ deviates from the LVE envelope (see Figure 8b). As shown in Figure 8c, the importance of confinement increases with the applied shear rate. This is also in line with the shear slit model, according to which the length scale of the confinement in the velocity gradient direction is the length of a shear strand whose size decreases with the shear rate. Second, an overshoot is observed in $R^2_{xx}(t)$. Figure 8c indicates that its importance increases with increasing shear rate. Interestingly, the time at the maximum of $R^2_{xx}(t)$, $\tau_{max(R^2_{xx})}$, corresponds to the time at which $R^2_{yy}(t)$ reaches a steady state (if we ignore a weak undershoot). Moreover, this time is longer than the time at which the transient viscosity reaches its maximum, $\tau_{max(\eta^+(t))}$.

As further discussed in Section III.II.IV.III., we also observe that before $\tau_{max(R^2_{xx})}$, $R^2_{xx}(t)$ increases while the chain is being confined, i.e., $R^2_{yy}(t)$ is decreasing. This can be attributed to the drag force exerted on the chain, which decreases with the chain confinement but stays larger than the drag force observed at longer times, in the steady regime, i.e., when the chains are confined. In fact, due to the gradual chain confinement, the increase of R^2_{xx} weakens progressively up to $t = \tau_{max(RR^2_{xx})}$, when it reaches its maximum value, and the chain reaches its confined state. At longer time, $t > \tau_{max(R^2_{xx})}$, R^2_{xx} decreases, and reaches its state−state value at a time close to the Rouse time, τ_R. As further discussed below, this suggests that the time needed to ensure that all the elastic modes of the chains are activated and to ensure that their size in the flow direction is adjusted to the applied force due to shear experienced by the chain in the confined state is well approximated by the Rouse time determined in the equilibrium state.

The first normal stress difference can also be determined from the simulations. As illustrated in Figure 9 for sample N50, the transient first normal stress coefficient $\Psi_1^+(t) = \frac{N_1^+}{\dot{\gamma}^2}$ (with $\dot{\gamma}$ = 0.01 τ_{LJ}^{-1}) and the mean square end-to-end distance in the flow direction $R^2_{xx}(t)$ are found to be proportional, as soon as the time is longer than $\tau_{advection}$. The correlation between maximum stretch and maximum $\Psi_1^+(t)$ in Figure 9 is consistent with the prediction of the shear slit model.

III.II.III. Steady Regime: Validation of the Shear Slit Model. In this section, we compare the predictions of the shear slit model with our experimental and simulation data in the steady-state regime. Both the steady-state viscosity and the confinement state of the chains are discussed.

III.II.III.I. Steady-State Shear Viscosity η_{steady}. According to the shear slit model, in the steady regime, a polymer chain

https://doi.org/10.1021/acs.macromol.5c00553
Macromolecules 2025, 58, 7062−7083

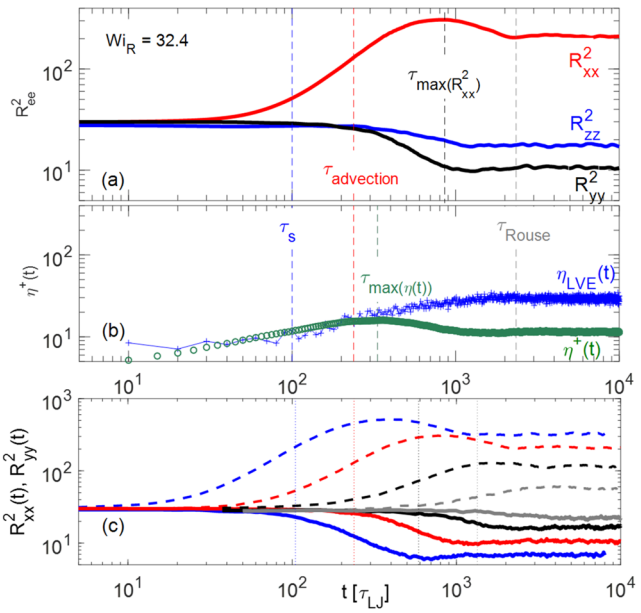

Figure 8. Simulation results for N50 as a function of time: (a) Average values of the square end-to-end distance in the flow direction (R^2_{xx}), the gradient direction (R^2_{yy}) and the vorticity direction (R^2_{zz}). (b) transient shear stress growth coefficient (green circles) at Wi_R = 32.4 ($\dot{\gamma}$ = 0.01 τ_{LJ}^{-1}). For comparison, the LVE envelope is also given (blue circles). (c) R^2_{xx} (dashed curves), R^2_{yy} (thick continuous curves) and $\tau_{advection}$ determined from eq 11 (vertical dashed lines) at Wi_R = 3.24 (gray), 10 (black), 32.4 (red), and 100 (blue). In this simulation, τ_R = 3240 τ_{LJ}, and $\dot{\gamma}$ = 0.001, 0.003, 0.01, and 0.03 τ_{LJ}^{-1}.

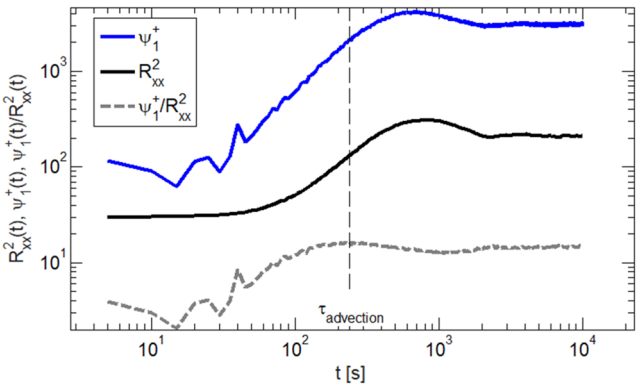

Figure 9. Simulation results comparing the first normal stress coefficient (blue solid curve) and the square of the end-to-end distance in the flow direction (black solid curve), for $\dot{\gamma}$ = 0.01 τ_{LJ}^{-1}. The dashed curve represents the ratio between the two curves. The vertical dashed line marks the advection time.

under high shear flow is confined inside a shear slit of size ξ_s, which only depends on the shear rate (see Figure 10).[41] The drag force exerted by the flow on the chain is reduced upon confinement due to the decrease of the relative velocity $\dot{\gamma}\xi_s$ (the shear rate $\dot{\gamma}$ times the length scale ξ_s of a shear strand). Following this concept, we define the shear strands, of mass M_S and of relaxation time $\tau_s = \tau_R(M_s) = \frac{1}{\dot{\gamma}}$, which represent the longest subchains in the velocity gradient direction that can relax during a time equal to the inverse shear rate. Thus, $M_s = M\sqrt{\left(\frac{1}{\dot{\gamma}}\right)/\tau_R} = M/\sqrt{\tau_R\dot{\gamma}}$ (see SI, Table S1). The relaxation time τ_s can also be defined as $\tau_s = \tau_0 g_s^2$, with g_s representing the number of Kuhn segments contained in a shear strand, i.e., $g_s = \frac{N}{p_s}$, with $p_s = \frac{M}{M_s} = \sqrt{\tau_R\dot{\gamma}}$ being the number of shear strands per chain. Thus, the size of a shear slit, $\xi_s \sim \sqrt{g_s}\,b$, with b, the length of a Kuhn segment. Based on this picture, we consider that the Rouse modes faster than the mode p_s (i.e., from $p = p_s + 1$ to $p_s + N$) are fully dissipative in the velocity gradient direction, while the slower modes (from p = 1 to p_s) cannot relax and consequently do not contribute to the steady shear viscosity.

This implies that, at $Wi_R > 1$, the steady shear viscosity of the chains should be equivalent to the steady shear viscosity η_{steady} (M_S) of a melt of shear strands of mass M_S. The latter can be easily determined, based on its corresponding Rouse relaxation modulus

$$G_{R,steady}(t) = \frac{\rho RT}{M_s}\sum_{p=1}^{g_s}\exp\left(-\frac{2p^2 t}{\tau_s}\right) \tag{4}$$

with $\tau_s = \tau_R(M_s) = \tau_0 g_s^2$ and using the value of τ_0 from Table 1. Therefore, the steady-state shear viscosity of the chains is equal to the steady-state viscosity of the shear strands, with $\eta^+_{shearstrand}(t)$ defined as

$$\eta^+_{shearstrand}(t) = \int_0^t G_{R,steady}(t - t')\mathrm{d}t' \tag{5}$$

Consequently, following ref 40, the steady viscosity of an unentangled linear polymer in a strong shear flow can be approximated as

$$\eta_{steady} \approx \frac{1.4\rho RT}{M_s}\sum_{p=1}^{g_s}\frac{\tau_s}{2p^2} = \frac{1.4\rho RT}{m_0}\frac{\sqrt{\tau_0\dot{\gamma}}}{1}\sum_{p=1}^{g_s}\frac{1}{2\dot{\gamma}p^2} \tag{6a}$$

where m_0 is the molar mass of a Kuhn segment. Note that in eq 6a, the numerical coefficient 1.4 was determined by the comparison of the scaling expression (eq 6a) with the data (see

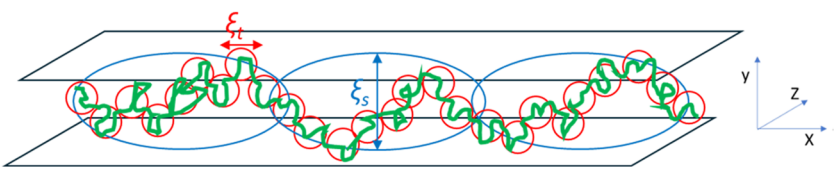

Figure 10. Shear slit model of a polymer in a nonlinear steady shear flow: Chain is stretched in the velocity x-direction into an extended array of tension blobs of size ξ_t with g_t Kuhn monomers in each blob. The chain is confined in the velocity gradient y-direction into a shear slit of size ξ_s (the y-size of shear strands) with g_s Kuhn monomers in each strand. The relaxation time of a shear strand is $\tau_s = \tau_0 g_s^2 = \dot{\gamma}^{-1}$ and its y- and z-sizes are $\xi_s \approx \xi_t(g_s/g_t)^{1/2}$. The shear strand is stretched in the velocity x-direction by the factor $(g_s/g_t)^{1/2}$ to a size $\xi_t(g_s/g_t)$. In the vorticity z-direction $R_{zz} \approx \xi_t(N/g_t)^{1/2} = bN^{1/2}$ the chain is almost unperturbed.

https://doi.org/10.1021/acs.macromol.5c00553
Macromolecules 2025, 58, 7062−7083

Figure 11). This numerical coefficient is independent of the molar mass of the sample and the shear rate.

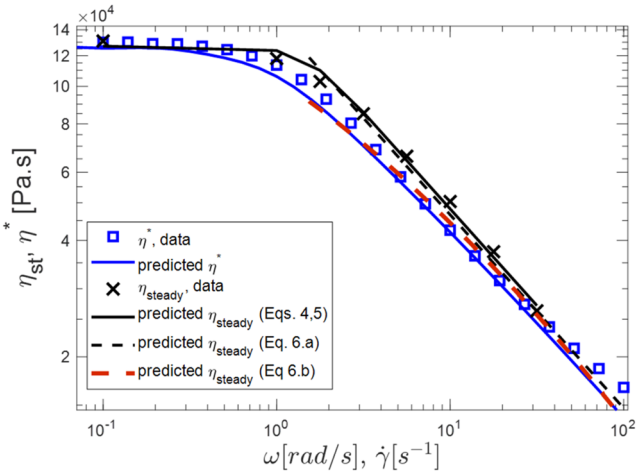

Figure 11. Comparison of the complex viscosity and the steady-state viscosity of PS30k at 130 °C with theoretical predictions.

Similarly, the steady viscosities can be predicted by using the model proposed by Colby et al.,[40] i.e., by considering that the slow Rouse modes of the whole chain do not contribute to the steady viscosity. According to this model, the apparent viscosity in steady shear is approximated by

$$\eta_{steady} = \frac{\rho RT}{M} \sum_{p=p_s+1}^{N} \frac{\tau_R}{p^2} \tag{6b}$$

To validate these expressions, we compare, in Figure 11, the theoretical steady-state viscosities with the experimental data obtained for PS30k at different shear rates. The respective theoretical and experimental complex viscosities are also shown (in blue), to assess the validity of the Cox−Merz rule.[69] The steady viscosity is well captured by eqs 4 and 5, as well as by the approximated expression based on the shear slit model (see eq 6a), which is only valid at high shear rates. This result thus supports the shear slit picture. The expression of Colby et al. (eq 6b) also gives a good description of the data. However, at intermediate shear rates, it underestimates the value of η_{st}, the shear thinning slope being slightly less steep than the one predicted with the shear slit model. This difference comes from the smoother transition of its relaxation modulus, from the Rouse relaxation modes to the terminal regime, due to the larger number of dissipating modes ($N - (p_s + 1)$ modes) which are considered in the calculation, compared to eq 6a (which only includes $g_s = N/p_s$ modes). Interestingly, a similar difference is observed between the experimental complex viscosity η^* and steady viscosity η_{st} as a function of the frequency and shear rate, respectively, leading to a slight failure of the Cox−Merz rule. Such a discrepancy has been already observed by other authors as well.[16,17,78] This comparison thus suggests that the complex viscosity is closer to eq 6b, while the steady shear viscosity data are in better agreement with the shear slit eq 6a.

A good agreement between our theoretical and experimental steady viscosities was also found for the other samples (see SI, Figure S8). This further validates the fact that at high shear rates, the steady-state viscosity is determined by the shear strands, with time $(\tau_R(M_s) = 1/\dot{\gamma})$. The same conclusion is also drawn from the simulations (see below). The steady-state viscosity is thus governed by the local equilibration of the chain in the gradient direction, taking place at the level of the shear strands, which are confined in a shear slit (see Figure 10). As discussed in Section III.II.IV, this mechanism is different from that governing the first normal stress difference, which depends on the chain tension in the velocity direction, and therefore varies with the molar mass of the chain.[41] It must be noted here that according to the shear slit model, the shear strand is defined by the deformation in the y direction. Nevertheless, in the following, we consider strands of $g_s = N/p_s$ monomers that can be stretched in the velocity direction (see Figure 10).

The shear slit picture is also consistent with the experimental rheo-dielectric data of Matsumiya et al.,[76,77] who observed that the end-to-end fluctuation time of unentangled polymer chains decreases with increasing shear rate. Indeed, as shown in SI (Figures S9 and S10), the shear slit model predicts that the relaxation time of the end-to-end vector of a chain in the gradient direction is proportional to the square of its size. This corresponds to a relaxation time which scales with $\dot{\gamma}^{-1/2}$, in agreement with the results obtained from both the rheo-dielectric measurements and the simulations. However, at the local level of a shear strand, we do not expect the Rouse time in the velocity gradient direction to be affected by the flow.

III.II.III.II. Steady Shear Mean-Square End-to-End Distance in the Gradient Direction $R^2_{yy,steady}$. We take advantage of the NEMD simulations to investigate how the chain configuration in the steady state depends on the shear rate and the molar mass of the polymer. In particular, the molecular picture of a chain composed of $p_s = \sqrt{\tau_R \dot{\gamma}}$ shear strands of size ξ_s in the velocity gradient direction (see Figure 10) is tested, based on the steady shear mean-square end-to-end distance $R^2_{yy,steady}$ of the chains, for different shear rates ($\dot{\gamma}$ = 0.003, 0.01 or 0.03 τ_{LJ}^{-1}) and different molar masses (N = 50 or N = 100) obtained from the simulation. According to this picture, the chain is always able to equilibrate at a length scale of a shear strand in the velocity gradient direction. The mean square size of a shear strand in the velocity gradient direction, ξ_s, is defined as

$$\xi_s = \sqrt{g_s b^2} = \sqrt{\frac{Nb^2}{p_s}} = \frac{R_{yy,0}}{(\tau_R \dot{\gamma})^{1/4}} = \frac{b}{(\tau_0 \dot{\gamma})^{1/4}} \tag{7}$$

with g_s, the number of Kuhn segments in a shear strand. It is independent of the molar mass of the chain. Similarly, the size of the shear slit is expected to be independent of the molar mass of the chain, and the steady-state root-mean-square end-to-end distance of the sheared chains in the velocity gradient direction, $R_{yy,steady} = \sqrt{\langle R^2_{yy,steady} \rangle}$ is expected to be proportional to the shear strand size, $R_{yy,\,steady} \propto \xi_s$.

The simulation results obtained for $R_{yy,steady}$ are shown in Figure 12. It is observed that at high shear rates, the data of N50 and N100 superimpose, confirming that in the steady-state regime, the chain confinement does not depend on the molar mass of the chains. This further validates the shear slit model with a chain equilibrated at the level of a shear strand in the y direction. The theoretical values of ξ_s (eq 7) are also shown by dashed lines in Figure 12. The proportionality between $R_{yy,steady}$ and ξ_s is observed in the simulations data, $R_{yy,steady} \cong 1.4\xi_s$. Note that this proportionality factor is similar to the prefactor needed in eq 6a. to quantitatively describe the experimental steady viscosity.

https://doi.org/10.1021/acs.macromol.5c00553
Macromolecules 2025, 58, 7062−7083

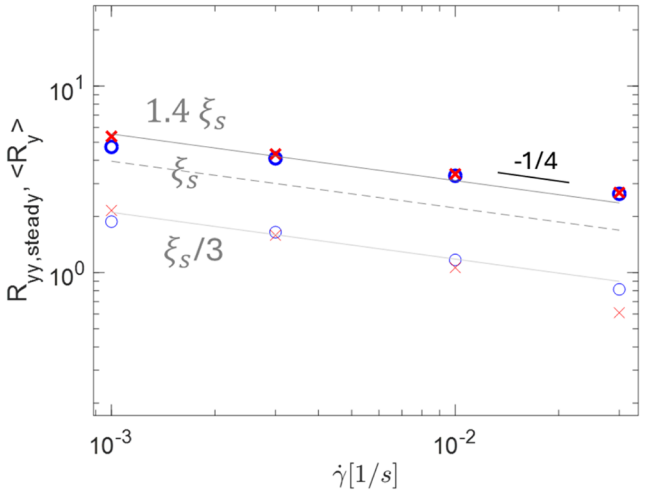

Figure 12. Steady-state root-mean-square end-to-end distance of sheared chains in the velocity gradient direction ($R_{yy,steady}$, thick symbols) and average value of the end-to-end vector of the chain in the velocity gradient direction $\langle R_y \rangle$ (thin symbols) as a function of $\dot{\gamma}$ = 0.001, 0.003, 0.01, and 0.03 τ_{LJ}^{-1}. Simulation results for N50 are blue (o) while for N100 are shown by red (X), The gray dashed line corresponds to ξ_s (eq 7), characterized by the power law dependence on shear rate $\xi_s \sim \dot{\gamma}^{-1/4}$ (slope of −1/4 on a log−log plot). The gray continuous lines correspond to ($R_{yy,steady} = 1.4\xi_s$) and to ($\langle R_y \rangle = \xi_s/3$).

Figure 12 also displays the steady-state average value of the end-to-end distance of the chain in the velocity gradient direction, $\langle R_y \rangle$. The average chain tension in the flow direction is expected to depend on this distance, while $R_{yy,steady}$ accounts for the fluctuations along the y axis, which determines the viscosity. $\langle R_y \rangle$ is relatively small compared to $R_{yy,steady}$ (with $\langle R_y \rangle \approx \xi_s/3$), however both distances are found to be proportional to shear slit size ξ_s.

These simulation results thus confirm the confinement of the chains in shear slits. As further discussed in Section III.II.IV.III., this confinement leads to a reduction of the drag force exerted on the chain, and thus, to a decrease of the steady-state viscosity and shear thinning properties.

III.II.III.III. Shear Slit Model vs Friction Reduction. Contrary to the shear slit model, some other studies[14,35,47] have attributed shear thinning of unentangled polymers to the reduction of the friction coefficient. Assuming that a test chain in the unentangled polymer can always be described by a Langevin-type model, these studies found that to fit the rheological and structural data from experiments and simulations, the friction coefficient should decrease with flow. However, this assumption could have oversimplified the multichain interactions in unentangled polymers. The shear slit model adopts a picture according to which a test chain is effectively confined a slit-like region due to the collective motion of the surrounding molecules under shear flow. This picture is intrinsically different from a Langevin model modified with its friction coefficient.

More importantly, the approaches based on the friction reduction concept do not predict the nonlinear shear rheology of unentangled polymers, and may only do so when

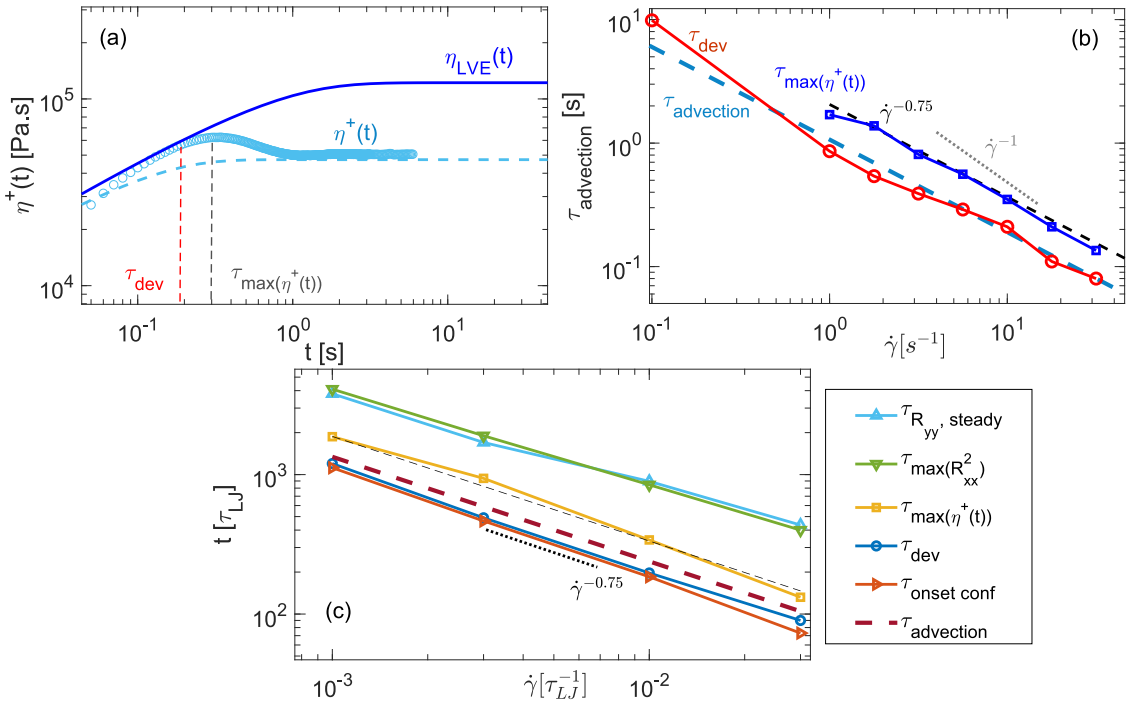

Figure 13. (a) Shear stress growth coefficient $\eta^+(t)$ of PS30k at 130 °C sheared at a constant rate $\dot{\gamma}$ = 10 s^{-1}. The dashed curve represents the theoretical prediction of $\eta^+(t)$ based on eqs 4 and 5, i.e., corresponding to the LVE response of a polymer melt composed of chains of mass M_s (or, equivalently, of chains of mass M confined in shear slits instantaneously formed at t = 0). (b) Dependence of τ_{dev} (red circles) and $\tau_{max(\eta^+(t))}$ (blue squares) on $\dot{\gamma}$. Their values have been determined from the experimental data for PS30k at 130 °C and are compared to the theoretical values of $\tau_{advection}$ (eq 11), see the light blue dashed line. The dashed black line corresponds to 2 $\tau_{advection}$. For comparison, the dotted gray line has a slope of −1. (c) The shear rate dependence of the characteristic times (defined in Figure 8) from simulation data of sample N50: $\tau_{R_{yy},steady}$ at which R_{yy} reaches its steady level, $\tau_{max(R_{xx}^2)}$ at which the maximum of R_{xx}^2 is reached, $\tau_{max(\eta^+)}$, τ_{dev}, and $\tau_{onsetconf}$ at which R_{yy}^2 starts to decrease are compared to the theoretical values of $\tau_{advection}$ (eq 11). The black dashed line corresponds to 1.4 $\tau_{advection}$.

https://doi.org/10.1021/acs.macromol.5c00553
Macromolecules 2025, 58, 7062−7083

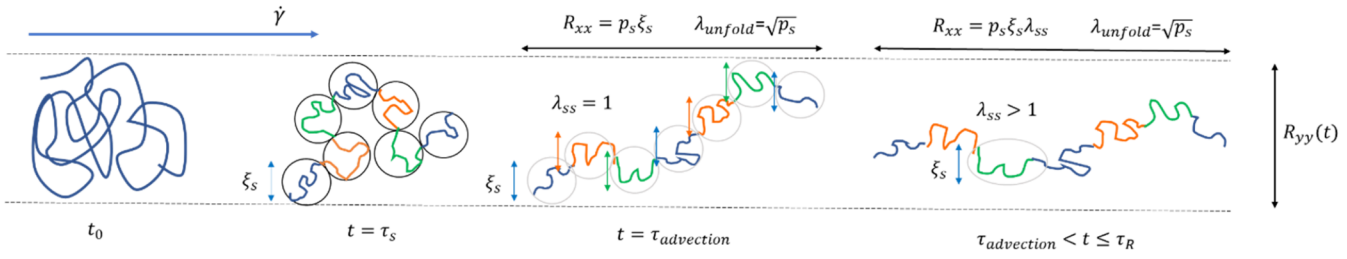

Figure 14. Schematic illustration of the chain extension λ_{chain}, λ_{unfold} and λ_{ss} (see text), and progressive chain confinement, from R_{yy} $(t = 0) = R_{yy,0}$ toward $R_{yy,steady} = \xi_s$ (not shown here, but illustrated in Figure 10).

incorporated into constitutive models (as done for example with entangled polymers[15]). On the contrary, using the concept of a shear strand, the shear slit model explicitly predicts the nonlinear shear rheology of unentangled polymers. It thus provides the possibility to be confronted and validated against experimental and simulation data.

Here, we stick to the concept that the friction coefficient is monomeric, which means that it relies on the molecular structure comparable to the size of a monomer. To observe a change in the monomeric friction coefficient ζ_0 in unentangled polymers, a chain needs to be stretched by a tension of magnitude kT/b, corresponding to the end-to-end distance of Nb. This means that at a moderate shear rate such that $Wi_R \geq 1$, where the size of the polymer chain in the flow direction is between $\sqrt{N}b$ and Nb, a reduction of monomeric friction coefficient is not expected. However, experimentally it has been confirmed that shear viscosity of unentangled polymers always starts decreasing from $Wi_R = 1$.[40,79] This drop of viscosity indicates that the reduction of flow dragging force takes place even if the local structure is almost unchanged. The shear slit model explains this effect as a decrease of the chain dimension in the flow gradient direction due to the effective confinement effect, so that the chain is less exposed to the flow. This is confirmed from the simulation data. Thus, this interpretation based on the shear slit model accounts for a more consistent molecular picture of the nonlinear shear rheology of unentangled polymers.

III.II.IV. Transient Regimes. In Section III.II.IV.I we extract characteristic times for different regimes from the time dependence of the shear stress growth coefficient $\eta^+(t)$ and of the mean-square end-to-end distance in the velocity gradient direction. We also discuss the advection time $\tau_{advection}$, and show that it corresponds to the time when the chains stop to deform affinely. Its value is found to be proportional to the other characteristic times. Then, in Section III.II,IV.II, we relate $\eta^+(t)$ to the chain confinement and propose a simple model to describe $\eta^+(t)$, based on $\tau_{advection}$. Finally, in Section III.II.IV.III, we discuss the evolution of the first and second normal forces differences, in relation to the evolution of $R^2_{xx}(t)$.

III.II.IV.I. Characteristic Times. From the experimental data of $\eta^+(t)$, two characteristic times can be extracted as illustrated in Figure 13a for a representative sample, PS30k, at 130 °C: τ_{dev}, marking the deviation of the transient curve from the linear viscoelastic envelope, and the time at the maximum of stress overshoot, $\tau_{max(\eta^+(t))}$. The criterion used to determine τ_{dev} was to consider the time at which the transient curve deviates by 5% from the LVE envelope, i.e., $\frac{\eta^+(t=\tau_{advection})}{\eta_{LVE}(t=\tau_{advection})} = 0.95$ (Figure 13a). Considering such a deviation allows obtaining results which do not depend on the experimental accuracy.

The time τ_{dev}, corresponding to the deviation of the transient curve from LVE is found to scale with the shear rate, as $\tau_{dev} \propto \dot{\gamma}^{-3/4}$ in both experiments (Figure 13b) and simulations (Figure 13c). This scaling suggests that the faster a chain is sheared, the larger is the strain $(\dot{\gamma}\tau_{dev} \sim (\tau_R\dot{\gamma})^{1/4})$ marking the deviation from the LVE envelope. Moreover, it is observed that the time at the maximum of the overshoot, $\tau_{max(\eta^+)}$ is also proportional to $\dot{\gamma}^{-3/4}$ in both experiments (Figure 13b) and simulations (Figure 13c), i.e., $\gamma_{max} \propto Wi_R^{1/4}$. This dependence is stronger than the power-law exponents of 0.14 and 0.17 observed in the experimental data for unentangled chains (Figure 6c). As illustrated in SI (Figure S11) for sample PS30k, this difference in slope may come from the uncertainties of the data at low shear rates, at which the maximum of the overshoot is not very well-defined, especially with low molar mass samples. As discussed below, this overshoot can be described as a competition between the increasing linear envelope and the shear force decreasing toward its steady-state value, taking place with the gradual confinement of the chain. As shown in Figure 13c for sample N50 and in Figure S12a for sample N100, the same scaling is found for τ_{dev} and $\tau_{max(\eta^+)}$ from the simulation data. Moreover, the time $\tau_{onsetconf}$ at which R^2_{yy} starts to decrease coincides with τ_{dev}, which further indicates that the deviation of $\eta^+(t)$ from the LVE envelope is a consequence of chain confinement. The confinement saturates at the time $\tau_{R_{yy},steady}$ at which the chains reach their steady level $R_{yy,steady}$. As further seen in Figure 15 below, $\tau_{R_{yy},steady}$ displays a slightly weaker dependence on the shear rate. This time also corresponds to the time $\tau_{max(R^2_{xx})}$ at which the maximum of R^2_{xx} is reached. As shown in Figure S12b, where the ratios of the different characteristic times to the advection time are plotted as a function of $\dot{\gamma}$, for both samples N50 and N100, the ratio $\frac{\tau_{max(R^2_{xx})}}{\tau_{advection}}$ varies with the molar mass of the chain, contrary to $\tau_{dev}/\tau_{advection}$ and $\tau_{max(\eta^+)}/\tau_{advection}$.

The other characteristic times of Figure 13c are related to the mean squared end-to-end distance R^2_{xx}, which are discussed in more detail in Section III.II.IV.III. In particular, it is observed that the time $\tau_{max(R^2_{xx})}$ coincides with $\tau_{R_{yy},steady}$.

The shear rate dependence of these times can be explained based on the chain confinement process. As illustrated in Figure 14, the evolution of the chain configuration due to the onset of the nonlinear shear flow can be described by taking the unperturbed size ξ_s of shear strands as the reference length scale. With this representation, it is convenient to divide the

https://doi.org/10.1021/acs.macromol.5c00553
Macromolecules 2025, 58, 7062−7083

total chain extension in the flow direction, $\lambda_{chain} = \frac{R_{xx}}{R_{xx,0}}$, into two contributions, λ_{unfold} and λ_{ss}, such as

$$\lambda_{chain} = \lambda_{unfold}\lambda_{ss} \tag{8}$$

$$\lambda_{unfold} = \frac{\min(R_{xx}, p_s\xi_s)}{R_{xx,0}} \tag{9}$$

$$\lambda_{ss} = \max\left(1, \frac{R_{xx}}{p_s\xi_s}\right) \tag{10}$$

The parameter λ_{unfold} describes the evolution of the chain, considering the shear strands as undeformable units. At short times following the application of shear, the chain configuration first evolves from a coil shape ($R_{xx} = R_{xx,0}$ and $\lambda_{chain} = \lambda_{unfold} = 1$) at $t = 0$ to the alignment of these unstretched shear strands, at $t = \tau_{advection}$ ($R_{xx} = p_s\ \xi_s$ and $\lambda_{chain} = \lambda_{unfold} = \frac{p_s\xi_s}{\sqrt{p_s}\xi_s} = \sqrt{p_s} = (\tau_R\dot{\gamma})^{1/4}$) where p_s is the number of shear strands per chain. As long as the shear strands are not fully aligned in the flow direction, λ_{ss}, which describes the stretch of a shear strand in the flow direction, is equal to 1. At later times, the shear strands extend and λ_{ss} becomes larger than 1, while λ_{unfold} saturates at its maximum value, $\sqrt{p_s}$.

Within this framework, we define the advection time $\tau_{advection}$, at which the end-to-end vector stops deforming affinely, as the time needed for a chain to deform by $\lambda_{unfold} = \sqrt{p_s} = (\tau_R\dot{\gamma})^{1/4}$ from random walk of shear strands to directed random walk of shear strands in the velocity direction (see Figure 14). Thus

$$\tau_{advection} = \frac{\sqrt{p_s}}{\dot{\gamma}} = \frac{(\tau_R\dot{\gamma})^{1/4}}{\dot{\gamma}} = (\tau_R)^{1/4}\dot{\gamma}^{-3/4} \tag{11}$$

is characterized by the same scaling as the one observed for most of the characteristic times defined in Figure 8 (see Figure 13b,c).

For an alternative description of the advection time $\tau_{advection}$, we define $g_{aff}(t)$, the number of Kuhn segments in the shortest strand, which is still deformed affinely with the flow at time t. Any strand containing more than $g_{aff}(t)$ Kuhn segments is advected affinely. The end-to-end length in the flow direction $r(t)$ of strands with $g_{aff}(t)$ Kuhn segments with initial root-mean-square end-to-end distance $r_0 \cong \sqrt{g_{aff}}b$ deformed affinely to $r(t) = r_0\dot{\gamma}t \cong \sqrt{g_{aff}}b\dot{\gamma}t$ These affine chain sections containing $g_{aff}(t)$ Kuhn segments are at the crossover between affine and nonaffine deformation (for time $t \geq \tau_s$). At this crossover condition, these chain sections are composed of an extended array of undeformed shear strands in the flow direction. Therefore, the end-to-end distance $r(t)$ of these affine chain sections should also be equal to the number of shear strands per affine section, g_{aff}/g_s, multiplied by the length of a shear strand, $\sqrt{g_s}b$. Considering that the two expressions of $r(t)$ are equivalent, we find

$$r(t) \cong \sqrt{g_{aff}}b\dot{\gamma}t \cong (g_{aff}/g_s)\sqrt{g_s}b \tag{12}$$

$$g_{aff} \approx g_s\left(\frac{t}{\tau_s}\right)^2 = \sqrt{\frac{1}{\tau_0\dot{\gamma}}}(\dot{\gamma}t)^2 \tag{13}$$

Since at the advection time, the whole chain is no longer able to deform affinely, i.e., $g_{aff}(\tau_{advection}) = N$, eq 11 is recovered.

The theoretical prediction of $\tau_{advection}$ from eq 11 is presented by the thick dashed line in Figure 13b,c without any adjustable parameters (i.e., with scaling coefficient of unity). A very good agreement is found between this theoretical time and the experimentally measured deviation times τ_{dev} (circles in Figure 13b,c). From the simulation data, it is also seen that $\tau_{advection}$ and τ_{dev} are similar, even though τ_{dev} is slightly lower. This difference, which becomes more pronounced with sample N100 (see SI, Figure S12) most probably comes from the criterion used to determine τ_{dev} from the experimental data.

Based on eq 11, it is also found that $\tau_{advection}$ is proportional to the square root of the molar mass of the chain: For a fixed shear rate, a longer chain needs more time to align its shear strands before these strands start to be extended in the flow direction. This N-dependence of $\tau_{advection}$ is verified in Figure 15b, which shows the transient simulation data of R^2_{yy}

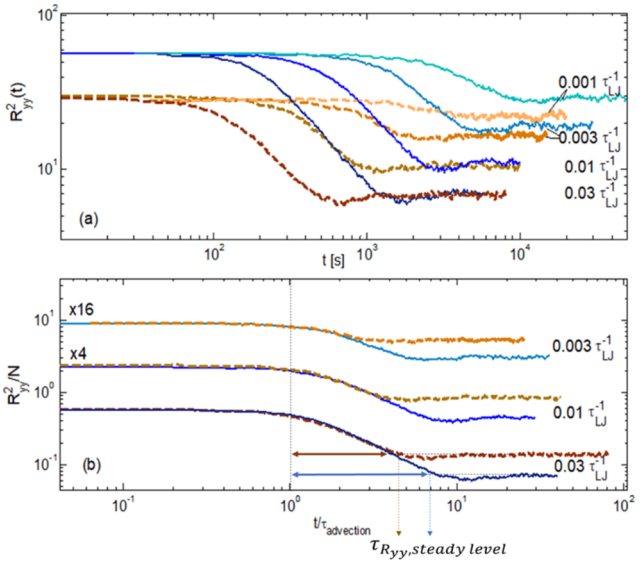

Figure 15. Simulation results for N50 (brown) and N100 (blue): (a) Average values of the square end-to-end distance in the velocity gradient direction (R^2_{yy}) as a function of t, at $\dot{\gamma}$ = 0.001, 0.003, 0.01, and 0.03 τ_{LJ}^{-1}. (b) R^2_{yy} normalized by N, as a function of $t/\tau_{advection}$. Data at 0.01 τ_{LJ}^{-1} and at 0.03 τ_{LJ}^{-1} were vertically shifted by 4 and 16, respectively. The double arrows indicate the ratio $\tau_{R_{yy,\ steady}}/\tau_{advection}$ at $\dot{\gamma}$ = 0.03 τ_{LJ}^{-1}.

normalized by N ($\propto R_0^2$), plotted as a function of $t/\tau_{advection}$, while Figure 15a presents the unshifted data. It is seen that the confinement process starts at $t/\tau_{advection} = 1$. Interestingly, it is observed that when chains of different molar masses are sheared at the same strain rate, the normalized curves plotted as a function of $t/\tau_{advection}$ superimpose at short times ($t \leq \tau_{advection}$), but also during their confinement process, i.e., between $t/\tau_{advection}$ and $\tau_{R_{yy,steady}}/\tau_{advection}$, when the steady-state regime is reached. This result suggests that during the confinement regime, $R_{yy}(t/\tau_{advection})$ stays proportional to N. Since during this process, $R_{yy}(t)$ decreases from $R_{yy,0} = \sqrt{p_s}\xi_s$ to $R_{yy,steady} = \xi_s$, with $R_{yy,steady}$ being independent of the molar mass of the chain (Figure 15a), the ratio

https://doi.org/10.1021/acs.macromol.5c00553
Macromolecules 2025, 58, 7062−7083

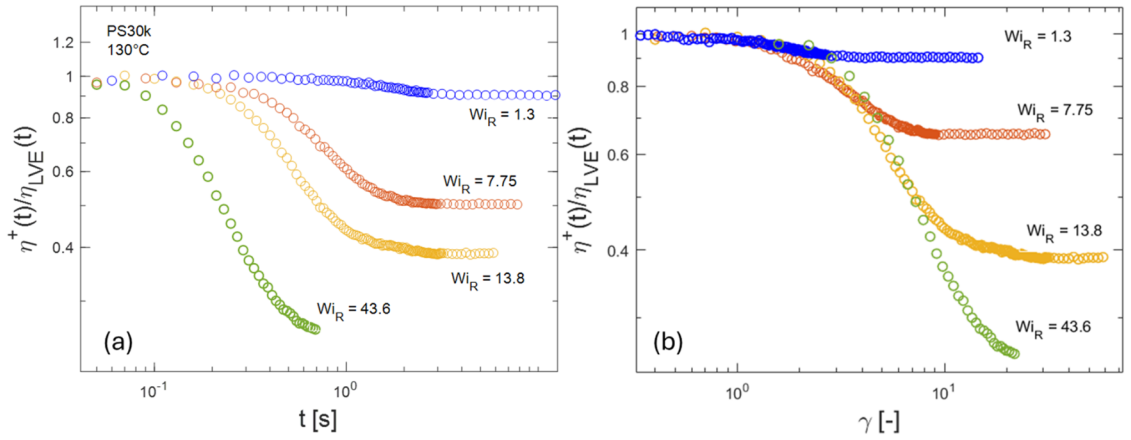

Figure 16. Experimental data: (a) Ratio $\eta^+(t)/\eta_{LVE}(t)$ as a function of time for sample PS30k at 130 °C. (b) the same $\eta^+(t)/\eta_{LVE}(t)$ data plotted against strain.

$\frac{R_{yy,0}}{R_{yy,steady}} = \sqrt{p_s} = (\tau_R\dot{\gamma})^{1/4}$ and consequently, the ratio $\tau_{R_{yy,steady}}/\tau_{advection}$ depends on the chain molar mass (Figure 15b).

Since in the y direction, the shear strands, which are able to equilibrate on a length scale of their size, ξ_s, can resist stretching, one can consider that they are undeformable for $\lambda < \lambda_{unfold}$. At short times, the chain unfolds to accommodate the flow, until it becomes a directed random walk of these effective (elastically resistant) shear strands ($\lambda_{unfold} = 1$) at time $t = \tau_{advection}$ (Figure 14). Then, their response at $t > \tau_{advection}$ becomes analogous to that of a finite extensible chain of shear strands. Similar to an almost fully stretched chain of Kuhn monomers[80,81] it begins to turn and get confined. The difference here is that shear strands are still elastic and can be further stretched in the flow direction (see below).

In the next Section, we show how the shear stress growth coefficient $\eta^+(t)$ is directly related to this chain confinement.

III.II.IV.II. Shear Stress Growth Coefficient $\eta^+(t)$. As mentioned above, before reaching its steady-state value, the stress growth coefficient goes through an overshoot. It is interesting to note that the overshoot (Figure 13a) can be seen as a crossover from the LVE envelope to η_{steady}: while at short times the increase of $\eta^+(t)$ with time does not depend on $\dot{\gamma}$ and follows the linear viscoelastic (LVE) envelope $\eta_{LVE}(t)$, at longer times, its increase slows down (softening) and goes through a maximum before reaching steady state. We attribute this crossover from affine response to a gradual confinement of the chain into a shear slit (see Section III.II.IV.I). This can be highlighted by looking at the shear stress growth coefficient normalized by the LVE envelope, $\eta^+(t)/\eta_{LVE}(t)$, as a function of time, shown in Figure 16a. In this representation, the overshoot of $\eta^+(t)$ totally disappears. The monotonic decrease of $\frac{\eta^+(t)}{\eta_{LVE}(t)}$ from unity to a steady-state value, which was found to start at $\tau_{advection} = (\tau_R\dot{\gamma})^{1/4}/\dot{\gamma}$, can be seen as a direct consequence of the shear-flow-induced chain confinement process.

When plotted as a function of the strain $\gamma = \dot{\gamma}t$ for the same number of Kuhn monomers N per chain, the $\eta^+(t)/\eta_{LVE}(t)$ data mostly overlap in the transient regime for different shear rates $\dot{\gamma}$ (Figure 16b). Similar overlap is also found for $R^2_{yy}(\gamma)$ as a function of the strain (see SI, Figure S13, for sample N50).

In order to describe this transient regime, we generalize the argument of de Gennes[82] (made for steady state) and suggest that the transient viscosity $\eta^+(t)$ is related to the square of the relative velocity, $(R_{yy}(t)\dot{\gamma})^2$ divided by the square of shear rate $\dot{\gamma}^2$ for unentangled polymers. This argument is validated by the simulation data of Figure 17: We observe that the ratio

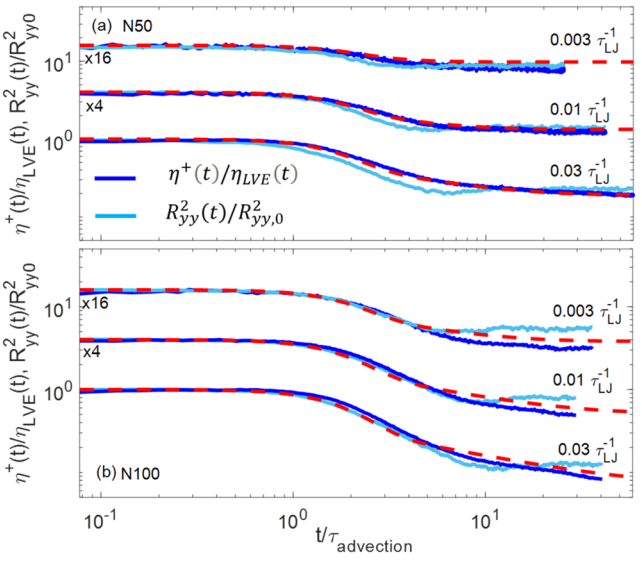

Figure 17. Simulation data: Comparison between the ratio $\eta^+(t)/\eta_{LVE}(t)$ (continuous blue curves) and $\left(\frac{R_{yy}(t)}{R_{yy,0}}\right)^2$ (continuous light blue curves) for samples N50 (a) and N100 (b), at different shear rates. For clarity, the curves at 0.01 τ_{LJ}^{-1} and 0.003 τ_{LJ}^{-1} have been vertically shifted by a factor 4 and 16, respectively. The simulation curves are compared to the predicted ratios determined from eqs 15−17. (Wi_R = 3240 $\tau_{LJ}\dot{\gamma}$ for N50 and 12960$\tau_{LJ}\dot{\gamma}$ for N100).

$\eta^+(t)/\eta_{LVE}(t)$ is very similar to the ratio of squares of shear slit size and undeformed chain size $\left(\frac{R_{yy}(t)}{R_{yy,0}}\right)^2$. This can also be confirmed based on the shear slit model at steady state, where $\left(\frac{R_{yy,steady}}{R_{yy,0}}\right)^2$, which is equal to $Wi_R^{-1/2}$, scales as the ratio of steady-state shear viscosity and zero-shear-rate viscosity, $\frac{\eta_{steady}}{\eta_0}$

https://doi.org/10.1021/acs.macromol.5c00553
Macromolecules 2025, 58, 7062−7083

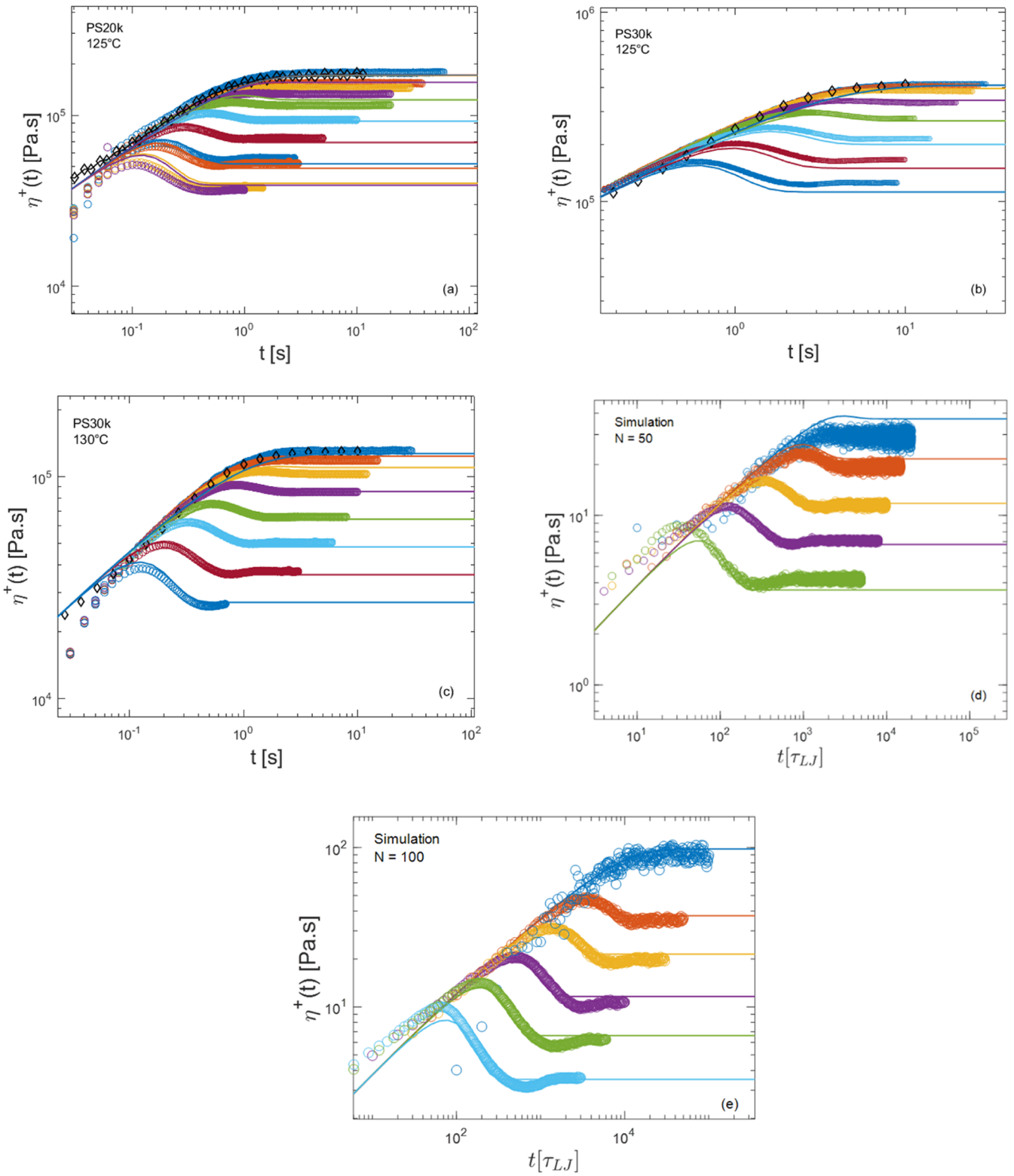

Figure 18. Comparison between experimental data (symbols) and predicted transient stress growth coefficient based on eqs 16 and 17 (continuous curves) for: (a) PS20k at 125 °C for shear rates from the top to the bottom: 0.1, 0.56, 1, 1.78, 3.16, 5.62, 10, 17.8, 20, 30, 31.6 s^{-1} (or, equivalently, at $Wi_R = \tau_R \dot{\gamma} = 1.3\dot{\gamma}$); (b) PS30k at 125 °C for deformation rates: 0.1, 0.178, 0.316, 0.562, 1, 1.78, 3.16, 5.62 s^{-1} ($Wi_R = \tau_R \dot{\gamma} = 4.46\ \dot{\gamma}$); (c) PS30k at 130 °C for deformation rates: 0.1, 1, 1.78, 3.16, 5.62, 10, 17.8, 31.6 s^{-1} ($Wi_R = \tau_R \dot{\gamma} = 1.38\ \dot{\gamma}$); (d, e) comparison between the predicted curves and the simulation data (symbols) for samples N50 (d) and N100 (e), for deformation rates: 0.001, 0.003, 0.01, 0.03 τ_{LJ}^{-1} ($Wi_R = 3240\tau_{LJ}\ \dot{\gamma}$ for N50 and $12960\tau_{LJ}\ \dot{\gamma}$ for N100).

https://doi.org/10.1021/acs.macromol.5c00553
Macromolecules 2025, 58, 7062−7083

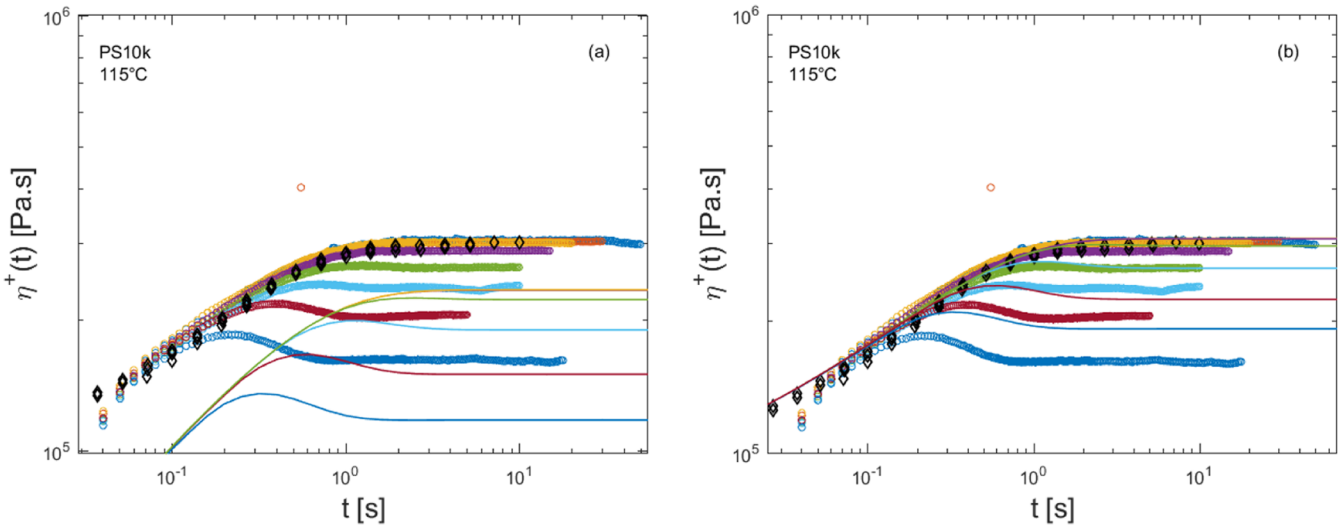

Figure 19. Transient viscosity of PS10k at 115 °C without (a) and with (b) the contribution of the glassy modes, for shear rates from the top to the bottom: 0.1 to 10 s^{-1}.

$$\frac{\eta_{steady}}{\eta_0} \approx \frac{\left(\frac{1.4\rho RT}{m_0}\sqrt{\tau_0\dot{\gamma}}\right)\left(\frac{1}{2\dot{\gamma}}\right)}{\frac{\rho RT}{M}\left(\frac{\tau_R}{2}\right)} = \frac{1.4}{\sqrt{\tau_R\dot{\gamma}}} \propto Wi_R^{-1/2} \tag{14}$$

This good overlap is found between the ratios of $\eta^+(t)/\eta_{LVE}(t)$ and $\left(\frac{R_{yy}(t)}{R_{yy,0}}\right)^2$, thus confirms that the overshoot in $\eta^+(t)$ can be interpreted as a consequence of the combined effect of an increase of the linear envelope $\eta_{LVE}(t)$ and a decrease of viscosity due to chain confinement.

To model these ratios, we then use a phenomenological function $A(t)$, to describe this crossover. Since the latter has been attributed to the chain confinement, the corresponding crossover time is expected to be a function of the advection time $\tau_{advection}$. As a first approach, we model it here with a Gaussian function

$$A(t) = \exp\left(-\left(\frac{t}{2\tau_{advection}}\right)^2\right) \tag{15}$$

As shown in SI (Figure S14), this transition function cannot be directly applied to the ratio $\eta^+(t)/\eta_{LVE}(t)$, leading to a too sharp transition. A similar conclusion can be drawn from the experimental data (Figure S15). Keeping the same formalism as in the linear regime, we rather relate the transition function $A(t)$ to the value of the relaxation modulus, to ensure accounting for the stress memory of the chains

$$\eta^+_{shearstrand}(t) = \int_0^t G_{R,LVE}(t-t')A(t')dt' + \int_0^t G_{R,steady}(t-t')(1-A(t'))dt' \tag{16}$$

with $G_{R,LVE}(t)$ and $G_{R,steady}(t)$ defined in eqs 1 and 4. Note that since in the steady state regime, $A(t)$ becomes 0, eq 17 well converges to eq 4. From eq 16, and defining the stress growth coefficient in the linear regime as

$$\eta_{LVE}(t) = \int_0^t G_{R,LVE}(t-t')dt' \tag{17}$$

the theoretical ratio $\eta^+_{shearstrand}(t)/\eta_{LVE}(t)$ is then determined, for both N50 and N100, and is compared to the simulation data in Figure 17. Very good agreement is obtained, which validates our approach.

It must be noted that the above equation is only valid for nonlinear shear flows ($Wi_R > 1$). An additional condition must be considered for the shear stress growth coefficient to be valid at lower shear rates, i.e., the shear slit has to be smaller than the original chain size ($\xi_S < R_{yy,0}$) for the chain to be confined in it, or equivalently, the molar mass of the shear strand, M_s, can never be larger than the molar mass of the entire chain, M. While this condition applies to all shear rates, it only affects the results at $Wi_R \leq 1$.

We then apply eq 16 to predict the theoretical shear stress growth coefficients of our samples deformed at different shear rates, in comparison to the experimental data (Figure 18a–c), or simulation data of N50 and N100 (Figure 18d,e), using the value of τ_0 given in Table 1 (with $\tau_R(M) = \tau_0 N^2$, $\tau_R(M_S) = \tau_0 g_S^2$, and $g_s = M/\sqrt{Wi_R}$), and accounting for the polydispersity (see Section II above and Figure SI2).

Despite some small discrepancies between the predicted and experimental curves, the model predicts the experimentally measured steady-state viscosity very well, both at high and low values of Wi_R. It is important to note that the experimental data are limited to a very small window on the transient viscosity scale (less than one decade). Consequently, they are very sensitive to small variations, especially at Wi_R slightly lower than 1. Indeed, in such a case, the model considers that all the Rouse modes are dissipative and contribute to the viscosity in a similar way as in the linear regime, while the experimental data already show a slight decrease in viscosity.

In Figure 19, we test this approach at a temperature close to T_g, and compare the predicted and experimental data for PS10k. While for PS20k and PS30k, the influence of the glassy modes is negligible, they have a very large effect on the LVE envelope, the position of the stress overshoot, and the steady viscosity for PS10k. This is mainly due to the short relaxation time of the chains, which are formed by only 14 Kuhn segments, leading to a rather small ratio between the Rouse relaxation time of the chains and the relaxation time of a Kuhn segment, τ_0 (see Figure 1a). If the glassy modes are simply

https://doi.org/10.1021/acs.macromol.5c00553
Macromolecules 2025, 58, 7062−7083

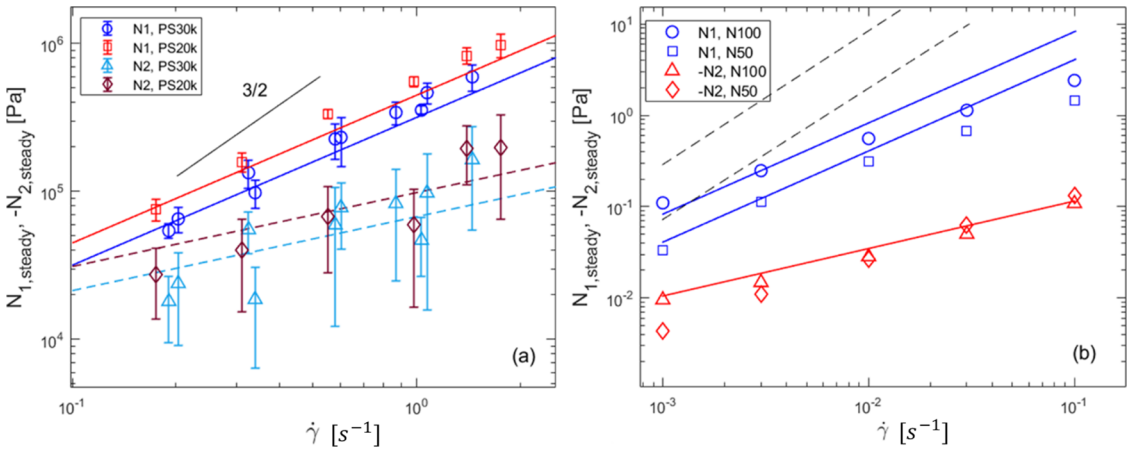

Figure 20. (a) Experimental results of $N_{1,\text{steady}}$ and $N_{2,\text{steady}}$ for samples PS20k and PS30k. Solid and dashed lines represent the equations $\left(N_1 = \frac{\rho RT}{M} 2\tau_R\dot{\gamma}\right)$ and $\left(N_2 = -\frac{1}{2}\frac{\rho RT}{M}\sqrt{\tau_R\dot{\gamma}}\right)$, respectively. The line with slope of 3/2 represents the scaling expected from the shear slit model. (b) Simulation results: Comparison between of $N_{1,\text{steady}}$ and $N_{2,\text{steady}}$ for sample N50 and sample N100, for $\dot{\gamma}$ = 0.001, 0.003, 0.01, 0.03, and 0.1 τ_{LJ}^{-1}. The dashed lines correspond to the equation $\left(N_1 = \frac{\rho RT}{M}(\tau_R\dot{\gamma})^{3/2}\right)$ while the blue continuous lines correspond to $(N_1 = \frac{\rho RT}{M}\tau_R\dot{\gamma}$, without the factor of 2 used in the solid lines in (a)). The red solid line corresponds to $\left(N_2 = -\frac{1}{2}\frac{\rho RT}{M}\sqrt{\tau_R\dot{\gamma}}\right)$.

added to the Rouse relaxation modes, as was done in the analysis of the linear viscoelasticity (see Section III.I.II), we observe that, while the prediction of the LVE is in very good agreement with the experimental data, the predicted transient viscosity is overestimated at the highest rates (Figure 19b). While this shows the limitations of our approach, it also highlights the importance of understanding the exact role of the glassy modes in the nonlinear regime. This question was investigated by Inoue et al.,[83] based on rheo-optical study of polystyrene chain under extension, and by Matsumiya et al.,[84] based on rheo-dielectric measurements. They found significant nonlinearities (thinning) of the glassy relaxation under extension even at very low Wi_R. As shown in SI (Figure S16), under high shear, a better agreement with the data is found if we consider that the characteristic time of a Kuhn segment, τ_0, is reduced by a factor 1.4. While a reduction of the glassy relaxation time is in line with the trend observed in ref 83, the influence of the flow stays, however, very limited, compared to the large effect seen by the authors of ref 83.

Finally, we remark that the simulation data for the shear stress growth coefficient exhibit an undershoot just before reaching the steady viscosity, similar to the experimental data (see Figure S3 in SI). In the case of entangled polymers, such an undershoot has been unambiguously detected and attributed to chain tumbling.[15,34,85,86] While accounting for this process is outside of the scope of the present manuscript, we observe here that an even more pronounced undershoot appears in $R_{yy}^2(t)$ (Figure 15), which cannot be easily attributed to tumbling. This result suggests that at very high rates, the shear strands can be temporarily slightly squeezed in the velocity gradient direction, before going back to their steady-state value.

III.II.IV.III. Mean-Square End-to-End Distance R_{xx}^2 and Normal Stress Differences N_1 and N_2. An important feature of the shear slit model is that it allows us to account for both the confinement in the velocity gradient direction (second normal stress difference) and the tension in the velocity direction (first normal stress difference). In this section, the experimental and simulation data are analyzed and discussed, based on the shear slit picture.

III.II.IV.IV. Steady-State Regime. As described in ref 41, in the steady regime, the chains are stretched in the flow direction, and the average size of tension blobs in the velocity (x) direction, ξ_t, is smaller than the size of the shear confinement slit in the velocity gradient (y) direction, ξ_s. As the chains are stretched in the x direction and confined in the y direction, the signs of the two normal stress differences are opposite. Moreover, the tension is stronger than confinement, therefore, the absolute value of the first normal stress difference is expected to be larger than of the second normal stress difference.

In the steady-state regime, the chain is under tension in the velocity direction due to drag force exerted on it from neighboring chains. This drag force is due to the relative velocity $\dot{\gamma}\xi_s$ exerted by the flow on the p_s shear strands if the latter have an average end-to-end distance ξ_s in the gradient direction. Since each of these shear strands is submitted to a friction $g_s\,\zeta_0$, with the monomeric friction ζ_0, the drag force $f_{\text{drag}} \cong N\zeta_0\dot{\gamma}\xi_s$. This drag force creates a tension in the chains, $f_{\text{tension}} \cong \frac{kT}{\xi_t}$. The corresponding tension blobs in the velocity direction have size $\xi_t \cong \frac{kT}{N\zeta_0\dot{\gamma}\xi_s}$.

Therefore, the additional stretch beyond advection increases with the Weissenberg number as $\lambda_{ss,st} = \frac{\xi_s}{\xi_t} \cong \xi_s^2\frac{\dot{\gamma}}{D} = \sqrt{Wi_R}$, where $D = \frac{kT}{N\zeta_0}$ is the diffusion coefficient of the chain, and $\tau_R \cong \frac{Nb^2}{D}$. The corresponding first normal stress difference, which is proportional to the number density of the tension blobs, is approximated as

$$N_1 = \frac{\rho RT}{M_t} \approx \frac{\rho RT}{M} p_s\lambda_{ss,st}^2 \approx \frac{\rho RT}{M}(\tau_R\dot{\gamma})^{3/2} \tag{18}$$

where M_t is the molar mass of a tension blob.[41] However, both experiments and simulations observe a weaker dependence, better described as

$$N_1 \cong \frac{\rho RT}{M} Wi_R \tag{19}$$

https://doi.org/10.1021/acs.macromol.5c00553
Macromolecules 2025, 58, 7062−7083

(see Figure 20). This discrepancy may have several origins, such as a nonuniform stretching along the chain backbone, from $\lambda_{ss} = 1$ for the shear strand at the chain extremities to larger stretch values in the middle of the chain. Since the chains are short, the influence of the outer shear strands may be large. The discrepancy observed with the experimental data may also come from the definition of the Rouse time, which has been determined at equilibrium and which may not be valid anymore in a nonequilibrium state.[77] In particular, if we consider that in the steady regime, the equilibration time of the monomeric tension in a shear strand is of the order of τ_R, only the faster Rouse modes $p \geq p_t$, with $\frac{\tau_R}{p_t^2} = \frac{1}{\dot{\gamma}}$ (thus $p_t = \sqrt{\tau_R \dot{\gamma}}$) contribute to the tension equilibration of a shear strand, while its slower modes, from $p = 1$ to p_t, are unable to relax, leading to p_t tension blobs per shear strand. In such a case, $N_1 \approx \frac{\rho RT}{M_s} p_t = \frac{\rho RT}{M} \tau_R \dot{\gamma}$, in agreement with the data.

This indicates the need for further model developments and additional experimental and simulation work. Note that if the correlation between the shear strands is ignored (i.e., the chain behaves as p_s sections of mass M_s confined in a shear slit) one would expect even a weaker shear rate dependence $N_1 \cong \frac{\rho RT}{M} Wi_R^{1/2}$.

The empirical rule of Laun is then tested on the steady-state values of N_1 for both N50 and N100 (SI, Figure S17). While it leads to the right scaling, the values found with the rule of Laun are underestimated by a factor 4.

The experimental data of the second normal stress N_2 are also shown in Figure 20. According to the shear slit model,[41] they must be negative and should be controlled by the average number of monomers in a shear strand, with

$$N_2 \approx -\frac{\rho RT}{M_S} = -\frac{\rho RT}{M}\sqrt{\tau_R \dot{\gamma}} \tag{20}$$

As shown in Figure 20, overall, the predicted curves well describe the data (if a prefactor 1/2 is considered), suggesting that N_2 is independent of M_w. The same conclusion is found from the simulation data (see also SI, Figure S18). Thus, N_2 is well described by the shear slit model, which also correctly describes the steady shear viscosity.

III.II.IV.V. Transient Regime. We can now look at the evolution of $R_{xx}(t)$ in the flow direction. The simulation data are presented in Figure 21a, while Figure 21b presents the normalized data, $\left(\frac{R_{xx}(t)}{p_s \xi_s}\right)^2 \approx \frac{R_{xx}^2(t)}{N^2\sqrt{\dot{\gamma}}}$ as a function of $t/\tau_{\text{advection}}$. The plot with this normalization for $t > \tau_{\text{advection}}$ describes the stretch state of a shear strand in the flow direction, $\lambda_{ss}(t)$. Indeed, at $t = \tau_{\text{advection}}$, the chains can be seen, in the x direction, as aligned arrays of shear strands. The latter are not yet extended ($\lambda_{ss} = 1$), meaning that $R_{xx}(t = \tau_{\text{advection}})$ should be equal to $p_s \xi_s$, i.e., should scale with $Wi_R^{1/4}$. Then, at time $t \geq \tau_{\text{advection}}$, $\lambda_{\text{unfold}} = \sqrt{p_s}$, (see eqs 8−10), and the shear strands start to stretch. In this regime ($t \geq \tau_{\text{advection}}$), the mean-squared end-to-end distance $R_{xx}^2(t)$ can be expressed as

$$R_{xx}^2(t) = R_{xx,0}^2(\lambda_{\text{unfold}}(t)\lambda_{ss}(t))^2 = R_{xx,0}^2(\sqrt{p_s}\lambda_{ss}(t))^2$$
$$\propto N((\tau_R\dot{\gamma})^{1/4}\lambda_{ss}(t))^2 \tag{21}$$

We validate this relationship in Figure 21b, where it is seen that all the curves cross each other at $t = \tau_{\text{advection}}$. This result

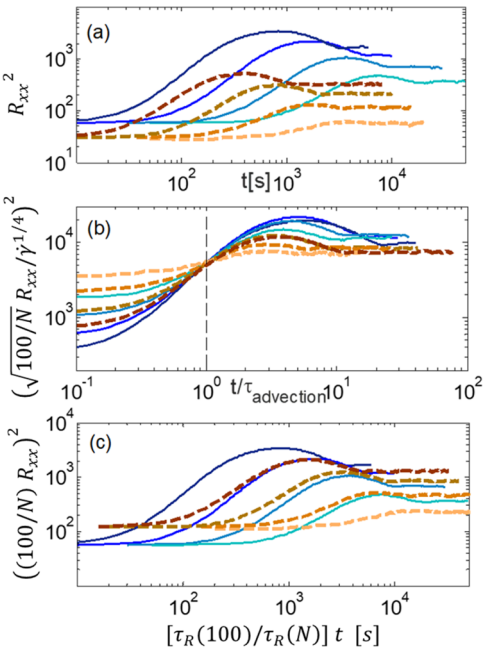

Figure 21. (a) Simulation results for N50 (brown−orange) and N100 (blue−green): (a) Average values of the square end-to-end distance in the flow direction R_{xx}^2 as functions of time (a) at $\dot{\gamma} = 0.001$, 0.003, 0.01, and 0.03 τ_{LJ}^{-1}. (b) Normalized data: $(R_{xx}^2\, N\dot{\gamma}^{-1/4})^2$ *vs* $t/\tau_{\text{advection}}$. (c) The data of N50 have been normalized to account for its shorter Rouse time and length, compared to sample N100.

demonstrates, once again, the importance of the advection time: at time $t < \tau_{\text{advection}}$, the chain deforms affinely and starts to orient and unfold to reach the alignment of its shear strands in the flow direction $\left(\lambda_{\text{unfold}} = \sqrt{p_s}\right)$ at $t = \tau_{\text{advection}}$, while at a longer time, the shear strands start to stretch in the flow direction $\left(\lambda_{\text{unfold}} = \sqrt{p_s},\ \text{and}\ \lambda_{ss} > 1\right)$, see Figure 14. As shear strands start to stretch, the confinement of the chain in the velocity gradient direction begins at $t > \tau_{\text{advection}}$.

In Figure 21b, one can also see that the overshoot observed in $R_{xx}^2(t)$ strongly depends on the shear rate applied: At a lower shear rate, the overshoot is much less pronounced, indicating that the shear strands are extending less before reaching their maximum stretch value. The presence of the overshoot in $R_{xx}^2(t)$ can be attributed to the fact that at early times, the chain is not yet confined in the shear slit and is experiencing a larger shear force. This larger force results in a larger chain extension. At longer times, the chain reaches its confined y-size reducing shear force and therefore reducing tension that results in the relaxation of its x-size to the steady-state value. This explanation is supported by the fact that the time $\tau_{\max(R_{xx}^2)}$ at the maximum of the overshoot of $R_{xx}^2(t)$ coincides with the time $\tau_{Ryy,\text{steady}}$ at which R_{yy}^2 reaches its steady-state value (see Figures 13 and S12).

After $\tau_{\max(R_{xx}^2)}$, $R_{xx}^2(t)$ decreases toward its steady value, as the Rouse modes are progressively elastically activated. Its steady state is reached at the time $t \approx \tau_R$ when all modes are activated. Thus, this reduction of the chain extension is attributed to the slow activation of the longer elastic Rouse modes: At time $t < \tau_R$, only the faster relaxation modes with index $p(t)$ between $\sqrt{\frac{\tau_R}{t}}$ and N are elastically activated (i.e., with $\tau_R\left(\frac{M}{p_{\text{act}}}\right) \leq t$).

https://doi.org/10.1021/acs.macromol.5c00553
Macromolecules 2025, 58, 7062−7083

Therefore, the chains can only equilibrate on the length scale of $g(t) \sim \sqrt{\frac{t}{\tau_0}}$, which determines the size of the longest chain segments that can elastically resist flow and can equilibrate their tension in the x-direction. This Rouse relaxation is confirmed in Figure 21c, which compares the equilibration process of samples N50 and N100. The R_{xx} data of N50 have been shifted vertically by a factor 2 to account for the fact that its length is twice shorter, and horizontally by a factor 4 to account for its shorter Rouse time. We see that plotted in this way, all the data superimpose between $\tau_{\max(R_{xx}^2)}$ and their steady regime. It must also be noted that the maximum time at which the $R_{xx}(t)$ reaches its steady state is similar to the Rouse time τ_R determined at equilibrium (see also Figure 8). Thus, from these data, contrary to ref 77, we cannot conclude that the shear flow has a large influence on this time.

The overshoot of $R_{xx}(t)$ can thus be divided into three parts: (i) its increase at times $t < \tau_{\text{advection}}$ due to the affine unfolding of the chains into arrays of shear strands, (ii) the stretch of the shear strands, up to the maximum of the chain size at the overshoot. The latter is reached at time $\tau_{\max(R_{xx}^2)}$, which also corresponds to the time $\tau_{R_{yy},\text{steady}}$ at which the chains are confined in shear slits (see Figures 13 and S12), (iii) finally, a partial relaxation of the stretch over very long interval up to τ_R.

IV. CONCLUSIONS

We investigated the nonlinear shear rheology of unentangled polymer melts. We used linear polystyrenes with molar masses of 10, 20, or 30 kg/mol. The measurements of shear and normal stresses were performed using cone-and-partitioned-plate rheometry. While the linear viscoelastic response could be accurately predicted with the Rouse model, in the nonlinear regime, the Cox−Merz rule was not fully validated, despite a universal thinning exponent of −0.5. We analyzed the nonlinear experimental results using the recent shear slit model[41] and molecular dynamics simulations. While the steady-state viscosity is governed by the size of the shear slit and is independent of the length of the chain, the first normal stress difference in the steady regime, which depends on the chain stretch, was found, based on both experimental data and simulations, to scale with the molar mass of the chain.

We then proposed a new molecular picture to explain the origin of the transient stress overshoot, based on the concept of the advection time $\tau_{\text{advection}}$ that marks the crossover between affine and nonaffine deformation and the start of the chain confinement. The advection time also corresponds to the time needed for a chain to deform by $\lambda_{\text{unfold}} = \sqrt{p_s} = (\tau_R\dot{\gamma})^{1/4}$ from random walk of shear strands to directed random walk of shear strands in the velocity direction, thus $\tau_{\text{advection}} = \tau_R^{1/4}\dot{\gamma}^{-3/4}$. This picture was validated by the mean square end-to-end distances $R_{xx}^2(t)$ and $R_{yy}^2(t)$ obtained from the simulations. Moreover, we showed that the time at the maximum of the overshoot, $\tau_{\max(\eta^+)}$ is also proportional to $\dot{\gamma}^{-3/4}$, i.e., $\gamma_{\max} \propto Wi_R^{1/4}$. Within the proposed picture, the overshoot observed in $\eta^+(t)$ is seen as a crossover from the LVE envelope to the steady-state regime.

Based on this picture, a simple model was developed, by combining Rouse relaxation modes, chain confinement to shear slit in the velocity gradient direction. The predictions of this model for shear viscosity are in excellent agreement with the experimental data and consistent with simulations. We then discussed the scaling observed for the first normal stress difference, $N_1 \approx \frac{\rho RT}{M} Wi_R$. The latter does not agree with the prediction of the shear slit model. While there are several ways to explain this discrepancy, its origin is not clear. On the contrary, the second normal stress coefficient N_2, which was determined by assuming that it is controlled by the average number of monomers in a shear strand, with $N_2 \approx -\frac{\rho RT}{M}\sqrt{\tau_R\dot{\gamma}}$, was found to be in very good agreement with the experimental and simulation data.

This work suggests that the shear slit model provides a reasonable framework to predict and discuss the shear properties of polymer melts. As a future work, it would be interesting to study how universal the advection process is. In particular, if we look into the Langevin models modified with different spring laws (but always finitely extensible), their steady-state solutions exhibit some universal properties at fast shear rates. There are some simple physical arguments to account for the effect of finite extensibility independent of the spring laws.[80] Thus, a universal process of advection in the transient regime should be possible, but needs to be checked further.

At this stage, the model proposed here has the advantage of being predictive, which is promising. However, we now need to extend this approach to entangled polymer melts and to binary blends, to further understand the influence of the chain environment and have investigate the possible effect of the shear rate on the interchain interactions. We also would like to link the shear slit molecular picture to the shear thinning described based on the concept of a reduction of friction.[14,47]

■ ASSOCIATED CONTENT

Supporting Information

The Supporting Information is available free of charge at https://pubs.acs.org/doi/10.1021/acs.macromol.5c00553.

Shifting of the dynamic oscillatory shear data; influence of the sample polydispersity (PDI) on the viscoelastic data; transient shear viscosity data; details on the MD simulations; shear slit model; influence of the glassy modes (PDF)

■ AUTHOR INFORMATION

Corresponding Authors

Dimitris Vlassopoulos − *Institute of Electronic Structure and Laser, FORTH, Heraklion 71110 Crete, Greece; Department of Materials Science & Engineering, University of Crete, Heraklion 71003 Crete, Greece;* orcid.org/0000-0003-0866-1930; Email: dvlasso@iesl.forth.gr

Michael Rubinstein − *Thomas Lord Department of Mechanical Engineering and Materials Science, Biomedical Engineering, Physics, and Chemistry, Duke University, Durham, North Carolina 27708-9976, United States; Institute for Chemical Reactions Design and Discovery, Hokkaido University, Sapporo 060-0808, Japan;* Email: mr351@duke.edu

Evelyne van Ruymbeke − *Bio- and Soft Matter (BSMA), Institute of Condensed Matter and Nanosciences, Université Catholique de Louvain, Louvain-la-Neuve B-1348, Belgium;* orcid.org/0000-0001-7633-0194; Email: evelyne.vanruymbeke@uclouvain.be

https://doi.org/10.1021/acs.macromol.5c00553
Macromolecules 2025, 58, 7062−7083

Authors

Maxime Dalne − *Bio- and Soft Matter (BSMA), Institute of Condensed Matter and Nanosciences, Université Catholique de Louvain, Louvain-la-Neuve B-1348, Belgium*

Salvatore Costanzo − *Department of Chemical, Materials and Production Engineering, University of Naples Frederico II, 80138 Naples, Italy;* orcid.org/0000-0003-1780-389X

Katerina Peponaki − *Institute of Electronic Structure and Laser, FORTH, Heraklion 71110 Crete, Greece; Department of Materials Science & Engineering, University of Crete, Heraklion 71003 Crete, Greece*

Nuofei Jiang − *Bio- and Soft Matter (BSMA), Institute of Condensed Matter and Nanosciences, Université Catholique de Louvain, Louvain-la-Neuve B-1348, Belgium;* orcid.org/0000-0002-6105-354X

Stelios Alexandris − *Institute of Electronic Structure and Laser, FORTH, Heraklion 71110 Crete, Greece*

Nino Grizzuti − *Department of Chemical, Materials and Production Engineering, University of Naples Frederico II, 80138 Naples, Italy;* orcid.org/0000-0001-5866-609X

Complete contact information is available at: https://pubs.acs.org/10.1021/acs.macromol.5c00553

Notes

The authors declare no competing financial interest.

■ ACKNOWLEDGMENTS

We are grateful to Christina Pyromali and Céline Hannecart for helpful discussions. We also thank the European network "SoftComp" for supporting the visit of S.C. to E.V.R. and of M.D. to D.V.. M.D. thanks the FNRS for funding. E.V.R. is Senior Research Associate of the FRS-FNRS. M.R. acknowledges financial support from the National Institutes of Health under Grant P01-HL164320.

■ REFERENCES

(1) Doi, M.; Edwards, S. F. *The Theory of Polymer Dynamics*; Clarendon Press: Oxford, 1986.

(2) Rouse, P. E. A Theory of the Linear Viscoelastic Properties of Dilute Solutions of Coiling Polymers. *J. Chem. Phys.* **1953**, *21* (7), 1272−1280.

(3) Dealy, J. M.; Read, D. J.; Larson, R. G. *Structure and Rheology of Molten Polymers: From Structure to Flow Behavior and Back Again*; Carl Hanser Verlag GmbH Co KG, 2018.

(4) McLeish, T. C. B. Tube Theory of Entangled Polymer Dynamics. *Adv. Phys.* **2002**, *51* (6), 1379−1527.

(5) Watanabe, H. Viscoelasticity and Dynamics of Entangled Polymers. *Prog. Polym. Sci.* **1999**, *24* (9), 1253−1403.

(6) Rubinstein, M.; Colby, R. H. *Polymer Physics*; Oxford University Press: New York, 2003; Vol. *23*.

(7) van Ruymbeke, E.; Liu, C.-Y.; Bailly, C. Quantitative Tube Model Predictions for the Linear Viscoelasticity of Linear Polymers. *Rheol. Rev.* **2007**, *39*, 53−134.

(8) van Ruymbeke, E.; Vlassopoulos, D. Macromolecular Rheology. *Macromol. Eng.* **2022**, 1−56.

(9) de Gennes, P. G. Reptation of a Polymer Chain in the Presence of Fixed Obstacles. *J. Chem. Phys.* **1971**, *55* (2), 572−579.

(10) Hua, C. C.; Schieber, J. D.; Venerus, D. C. Segment Connectivity, Chain-Length Breathing, Segmental Stretch, and Constraint Release in Reptation Models. III. Shear Flows. *J. Rheol.* **1999**, *43* (3), 701−717.

(11) Schieber, J. D.; Neergaard, J.; Gupta, S. A Full-Chain, Temporary Network Model with Sliplinks, Chain-Length Fluctuations, Chain Connectivity and Chain Stretching. *J. Rheol.* **2003**, *47* (1), 213−233.

(12) Masubuchi, Y.; Takimoto, J.-I.; Koyama, K.; Ianniruberto, G.; Marrucci, G.; Greco, F. Brownian Simulations of a Network of Reptating Primitive Chains. *J. Chem. Phys.* **2001**, *115* (9), 4387−4394.

(13) Ianniruberto, G.; Marrucci, G. Origin of Shear Thinning in Unentangled Polystyrene Melts. *Macromolecules* **2020**, *53* (4), 1338−1345.

(14) Ianniruberto, G.; Brasiello, A.; Marrucci, G. Simulations of Fast Shear Flows of PS Oligomers Confirm Monomeric Friction Reduction in Fast Elongational Flows of Monodisperse PS Melts As Indicated by Rheooptical Data. *Macromolecules* **2012**, *45* (19), 8058−8066.

(15) Costanzo, S.; Huang, Q.; Ianniruberto, G.; Marrucci, G.; Hassager, O.; Vlassopoulos, D. Shear and Extensional Rheology of Polystyrene Melts and Solutions with the Same Number of Entanglements. *Macromolecules* **2016**, *49* (10), 3925−3935.

(16) Rathinaraj, J. D. J.; Keshavarz, B.; McKinley, G. H. Why the Cox−Merz Rule and Gleissle Mirror Relation Work: A Quantitative Analysis Using the Wagner Integral Framework with a Fractional Maxwell Kernel. *Phys. Fluids* **2022**, *34* (3), No. 033106.

(17) Snijkers, F.; Vlassopoulos, D. Appraisal of the Cox-Merz Rule for Well-Characterized Entangled Linear and Branched Polymers. *Rheol. Acta* **2014**, *53* (12), 935−946.

(18) Wang, S.-Q. *Nonlinear Polymer Rheology: Macroscopic Phenomenology and Molecular Foundation*; John Wiley & Sons, 2018.

(19) Ianniruberto, G.; Marrucci, G.; Masubuchi, Y. Melts of Linear Polymers in Fast Flows. *Macromolecules* **2020**, *53* (13), 5023−5033.

(20) Huang, Q.; Alvarez, N. J.; Matsumiya, Y.; Rasmussen, H. K.; Watanabe, H.; Hassager, O. Extensional Rheology of Entangled Polystyrene Solutions Suggests Importance of Nematic Interactions. *ACS Macro Lett.* **2013**, *2* (8), 741−744.

(21) Huang, Q.; Hengeller, L.; Alvarez, N. J.; Hassager, O. Bridging the Gap between Polymer Melts and Solutions in Extensional Rheology. *Macromolecules* **2015**, *48* (12), 4158−4163.

(22) Matsumiya, Y.; Watanabe, H.; Masubuchi, Y.; Huang, Q.; Hassager, O. Nonlinear Elongational Rheology of Unentangled Polystyrene and Poly(*p* - *Tert*- Butylstyrene) Melts. *Macromolecules* **2018**, *51* (23), 9710−9729.

(23) Shahid, T.; Clasen, C.; Oosterlinck, F.; van Ruymbeke, E. Diluting Entangled Polymers Affects Transient Hardening but Not Their Steady Elongational Viscosity. *Macromolecules* **2019**, *52* (6), 2521−2530.

(24) Hannecart, C.; Shahid, T.; Vlassopoulos, D.; Oosterlinck, F.; Clasen, C.; van Ruymbeke, E. Decoding the Steady Elongational Viscosity of Monodisperse Linear Polymers Using Tube-Based Modeling. *J. Rheol.* **2022**, *66* (1), 197−218.

(25) Stratton, R. A. Non-Newtonian Flow in Polymer Systems with No Entanglement Coupling. *Macromolecules* **1972**, *5* (3), 304−310.

(26) Santangelo, P. G.; Roland, C. M. Interrupted Shear Flow of Unentangled Polystyrene Melts. *J. Rheol.* **2001**, *45* (2), 583−594.

(27) Schweizer, Th. Comparing Cone-Partitioned Plate and Cone-Standard Plate Shear Rheometry of a Polystyrene Melt. *J. Rheol.* **2003**, *47* (4), 1071−1085.

(28) Snijkers, F.; Vlassopoulos, D. Cone-Partitioned-Plate Geometry for the ARES Rheometer with Temperature Control. *J. Rheol.* **2011**, *55* (6), 1167−1186.

(29) Costanzo, S.; Ianniruberto, G.; Marrucci, G.; Vlassopoulos, D. Measuring and Assessing First and Second Normal Stress Differences of Polymeric Fluids with a Modular Cone-Partitioned Plate Geometry. *Rheol. Acta* **2018**, *57* (5), 363−376.

(30) Aoyagi, T.; Doi, M. Molecular Dynamics Simulation of Entangled Polymers in Shear Flow. *Comput. Theor. Polym. Sci.* **2000**, *10* (3), 317−321.

(31) Baig, C.; Mavrantzas, V. G.; Kröger, M. Flow Effects on Melt Structure and Entanglement Network of Linear Polymers: Results from a Nonequilibrium Molecular Dynamics Simulation Study of a Polyethylene Melt in Steady Shear. *Macromolecules* **2010**, *43* (16), 6886−6902.

(32) Kim, J. M.; Edwards, B. J.; Keffer, D. J.; Khomami, B. Dynamics of Individual Molecules of Linear Polyethylene Liquids under Shear:

Atomistic Simulation and Comparison with a Free-Draining Bead-Rod Chain. *J. Rheol.* **2010**, *54* (2), 283−310.
(33) Dambal, A.; Kushwaha, A.; Shaqfeh, E. S. G. Slip-Link Simulations of Entangled, Finitely Extensible, Wormlike Chains in Shear Flow. *Macromolecules* **2009**, *42* (18), 7168−7183.
(34) Nafar Sefiddashti, M. H.; Edwards, B. J.; Khomami, B. Individual Chain Dynamics of a Polyethylene Melt Undergoing Steady Shear Flow. *J. Rheol.* **2015**, *59* (1), 119−153.
(35) Jiang, N.; van Ruymbeke, E. Variation of Spring Stiffness, Monomeric Friction, and Brownian Intensity in the Simulation System of Unentangled Melt under Steady Flow. *Macromolecules* **2023**, *56* (8), 2911−2929.
(36) Galvani Cunha, M. A.; Olmsted, P. D.; Robbins, M. O. Probing the Nonequilibrium Dynamics of Stress, Orientation, and Entanglements in Polymer Melts with Orthogonal Interrupted Shear Simulations. *J. Rheol.* **2022**, *66* (3), 619−637.
(37) Jiang, N. Potential Universal Extensional Rheology in Concentrated Polymeric Liquids. *Macromolecules* **2024**, *57* (11), 5520−5532.
(38) Yasuda, K.; Armstrong, R. C.; Cohen, R. E. Shear Flow Properties of Concentrated Solutions of Linear and Star Branched Polystyrenes. *Rheol. Acta* **1981**, *20* (2), 163−178.
(39) Dealy, J. M.; Wang, J. *Melt Rheology and Its Applications in the Plastics Industry*; Springer, 2013.
(40) Colby, R. H.; Boris, D. C.; Krause, W. E.; Dou, S. Shear Thinning of Unentangled Flexible Polymer Liquids. *Rheol. Acta* **2007**, *46* (5), 569−575.
(41) Parisi, D.; Costanzo, S.; Jeong, Y.; Ahn, J.; Chang, T.; Vlassopoulos, D.; Halverson, J. D.; Kremer, K.; Ge, T.; Rubinstein, M.; Grest, G. S.; Srinin, W.; Grosberg, A. Y. Nonlinear Shear Rheology of Entangled Polymer Rings. *Macromolecules* **2021**, *54* (6), 2811−2827.
(42) Moreira, L. A.; Zhang, G.; Müller, F.; Stuehn, T.; Kremer, K. Direct Equilibration and Characterization of Polymer Melts for Computer Simulations. *Macromol. Theory Simul.* **2015**, *24* (5), 419−431.
(43) Everaers, R.; Karimi-Varzaneh, H. A.; Fleck, F.; Hojdis, N.; Svaneborg, C. Kremer−Grest Models for Commodity Polymer Melts: Linking Theory, Experiment, and Simulation at the Kuhn Scale. *Macromolecules* **2020**, *53* (6), 1901−1916.
(44) Groot, R. D.; Warren, P. B. Dissipative Particle Dynamics: Bridging the Gap between Atomistic and Mesoscopic Simulation. *J. Chem. Phys.* **1997**, *107* (11), 4423−4435.
(45) Masubuchi, Y.; Takata, H.; Amamoto, Y.; Yamamoto, T. Relaxation of Rouse Modes for Unentangled Polymers Obtained by Molecular Simulations. *Nihon Reoroji Gakkaishi* **2018**, *46*, 171−178.
(46) Cho, S.; Kim, J. M.; Baig, C. Scaling Characteristics of Rotational Dynamics and Rheology of Linear Polymer Melts in Shear Flow. *Macromolecules* **2020**, *53* (8), 3030−3041.
(47) Watanabe, H.; Matsumiya, Y.; Sato, T. Revisiting Nonlinear Flow Behavior of Rouse Chain: Roles of FENE, Friction-Reduction, and Brownian Force Intensity Variation. *Macromolecules* **2021**, *54* (8), 3700−3715.
(48) Narimissa, E.; Wagner, M. Modeling Nonlinear Rheology of Unentangled Polymer Melts Based on a Single Integral Constitutive Equation. *J. Rheol.* **2020**, *64*, 129−140.
(49) Poh, L.; Narimissa, E.; Wagner, M. H. Universality of Steady Shear Flow of Rouse Melts. *Rheol. Acta* **2020**, *59* (10), 755−763.
(50) Wagner, M. H.; Liu, S.; Huang, Q. The Effect of Rotationality on Nonlinear Shear Flow of Polymer Melts and Solutions. *Rheol. Acta* **2024**, *63* (8), 573−584.
(51) Pincus, P. Excluded Volume Effects and Stretched Polymer Chains. *Macromolecules* **1976**, *9* (3), 386−388.
(52) Pierleoni, C.; Ryckaert, J.-P. Deformation and Orientation of Flexible Polymers in Solution under Shear Flow: A New Picture for Intermediate Reduced Shear Rates. *Macromolecules* **1995**, *28* (14), 5097−5108.
(53) Taghipour, H.; Costanzo, S.; Vlassopoulos, D.; van Ruymbeke, E.; Hawke, L. G. D. Entangled Linear Polymers in Fast Shear Flows: Comparison of Tube-Model Predictions and Experimental Data. *J. Rheol.* **2021**, *65* (6), 1111−1137.
(54) Shchetnikava, V.; Slot, J.; van Ruymbeke, E. Comparative Analysis of Different Tube Models for Linear Rheology of Monodisperse Linear Entangled Polymers. *Polymers* **2019**, *11* (5), No. 754.
(55) van Ruymbeke, E.; Nielsen, J.; Hassager, O. Linear and Nonlinear Viscoelastic Properties of Bidisperse Linear Polymers: Mixing Law and Tube Pressure Effect. *J. Rheol.* **2010**, *54* (5), 1155−1172.
(56) Costanzo, S.; Pasquino, R.; Läuger, J.; Grizzuti, N. Milligram Size Rheology of Molten Polymers. *Fluids* **2019**, *4* (1), No. 28.
(57) Laukkanen, O.-V. Small-Diameter Parallel Plate Rheometry: A Simple Technique for Measuring Rheological Properties of Glass-Forming Liquids in Shear. *Rheol. Acta* **2017**, *56* (7), 661−671.
(58) Alexandris, S.; Peponaki, K.; Petropoulou, P.; Sakellariou, G.; Vlassopoulos, D. Linear Viscoelastic Response of Unentangled Polystyrene Bottlebrushes. *Macromolecules* **2020**, *53* (10), 3923−3932.
(59) Costanzo, S.; Parisi, D.; Schweizer, T.; Vlassopoulos, D. REVIEW: Nonlinear Shear Rheometry: Brief History, Recent Progress, and Challengesa). *J. Rheol.* **2024**, *68* (6), 1013−1036.
(60) Inoue, T.; Okamoto, H.; Osaki, K. Birefringence of Amorphous Polymers. 1. Dynamic Measurement on Polystyrene. *Macromolecules* **1991**, *24* (20), 5670−5675.
(61) Osaki, K.; Okamoto, H.; Inoue, T.; Hwang, E.-J. Molecular Interpretation of Dynamic Birefringence and Viscoelasticity of Amorphous Polymers. *Macromolecules* **1995**, *28* (10), 3625−3630.
(62) Ianniello, V.; Costanzo, S. Linear and Nonlinear Shear Rheology of Nearly Unentangled H-Polymer Melts and Solutions. *Rheol. Acta* **2022**, *61*, 667−679.
(63) Ferry, J. D. *Viscoelastic Properties of Polymers*, 3rd ed.; Wiley, 1980.
(64) Liu, C.-Y.; He, J.; Keunings, R.; Bailly, C. New Linearized Relation for the Universal Viscosity−Temperature Behavior of Polymer Melts. *Macromolecules* **2006**, *39* (25), 8867−8869.
(65) Walsh, D.; Zoller, P. *Standard Pressure Volume Temperature Data for Polymers*; CRC Press, 1995.
(66) Benallal, A.; Marin, G.; Montfort, J. P.; Derail, C. Linear Viscoelasticity Revisited: The Relaxation Function of Monodisperse Polymer Melts. *Macromolecules* **1993**, *26* (26), 7229−7235.
(67) Ngai, K. L.; Plazek, D. J.; Deo, S. S. Physical Origin of the Anomalous Temperature Dependence of the Steady-State Compliance of Low Molecular Weight Polystyrene. *Macromolecules* **1987**, *20* (12), 3047−3054.
(68) Ngai, K. L.; Plazek, D. J.; Rendell, R. W. Some Examples of Possible Descriptions of Dynamic Properties of Polymers by Means of the Coupling Model. *Rheol. Acta* **1997**, *36* (3), 307−319.
(69) Cox, W. P.; Merz, E. H. Correlation of Dynamic and Steady Flow Viscosities. *J. Polym. Sci.* **1958**, *28* (118), 619−622.
(70) Wang, S.-Q. Nonlinear Rheology of Entangled Polymers at Turning Point. *Soft Matter* **2015**, *11* (8), 1454−1458.
(71) Xie, S.-J.; Schweizer, K. S. Consequences of Delayed Chain Retraction on the Rheology and Stretch Dynamics of Entangled Polymer Liquids under Continuous Nonlinear Shear Deformation. *Macromolecules* **2018**, *51* (11), 4185−4200.
(72) Schweizer, T. Measurement of the First and Second Normal Stress Differences in a Polystyrene Melt with a Cone and Partitioned Plate Tool. *Rheol. Acta* **2002**, *41* (4), 337−344.
(73) Schweizer, T.; Bardow, A. The Role of Instrument Compliance in Normal Force Measurements of Polymer Melts. *Rheol. Acta* **2006**, *45* (4), 393−402.
(74) Laun, H. M. Prediction of Elastic Strains of Polymer Melts in Shear and Elongation. *J. Rheol.* **1986**, *30* (3), 459−501.
(75) Everaers, R.; Sukumaran, S. K.; Grest, G. S.; Svaneborg, C.; Sivasubramanian, A.; Kremer, K. Rheology and Microscopic Topology of Entangled Polymeric Liquids. *Science* **2004**, *303* (5659), 823−826.

https://doi.org/10.1021/acs.macromol.5c00553
Macromolecules 2025, 58, 7062−7083

(76) Matsumiya, Y.; Sato, T.; Chen, Q.; Watanabe, H. Rheo-Dielectric Behavior of Unentangled Poly(Butylene Oxide) under Steady Shear: Preliminary Evaluation of Non-Equilibrium Parameters at the Onset of Nonlinearity. *Nihon Reoroji Gakkaishi* **2022**, *50* (5), 371−385.
(77) Matsumiya, Y.; Sato, T.; Chen, Q.; Watanabe, H. Rouse Analysis of Nonlinear Rheology of Unentangled Polymer Melts under Fast Shear: Viscoelastic Response to Superposed Oscillatory Strain. *Macromolecules* **2023**, *56* (8), 2930−2938.
(78) Pattamaprom, C.; Larson, R. G. Constraint Release Effects in Monodisperse and Bidisperse Polystyrenes in Fast Transient Shearing Flows. *Macromolecules* **2001**, *34* (15), 5229−5237.
(79) Krause, W. E.; Tan, J. S.; Colby, R. H. Semidilute Solution Rheology of Polyelectrolytes with No Added Salt. *J. Polym. Sci., Part B: Polym. Phys.* **1999**, *37* (24), 3429−3437.
(80) Subbotin, A.; Semenov, A.; Manias, E.; Hadziioannou, G.; ten Brinke, G. Nonlinear Rheology of Polymer Melts under Shear Flow. *Macromolecules* **1995**, *28* (11), 3898−3900.
(81) Semenov, A. N.; Subbotin, A. V.; Hadziioannou, G.; ten Brinke, G.; Manias, E.; Doi, M. Nonlinear Dynamics of Melted Polymer Layers. *Macromol. Symp.* **1997**, *121* (1), 175−186.
(82) de Gennes, P. G. Molten Polymers in Strong Flows: A Nonclassical Proposal. *MRS Bull.* **1991**, *16* (1), 20−21.
(83) Inoue, T.; Ryu, D.-S.; Osaki, K. A Rheo-Optical Study on Polystyrene under Large Tensile Deformation around the Glass Transition Temperature. *Macromolecules* **1998**, *31* (20), 6977−6983.
(84) Matsumiya, Y.; Watanabe, H.; Inoue, T.; Osaki, K.; Yao, M.-L. Rheo-Dielectric Behavior of Oligostyrene and Polyisoprene. *Macromolecules* **1998**, *31* (22), 7973−7975.
(85) Xu, X.; Chen, J.; An, L. Shear Thinning Behavior of Linear Polymer Melts under Shear Flow via Nonequilibrium Molecular Dynamics. *J. Chem. Phys.* **2014**, *140* (17), No. 174902.
(86) Parisi, D.; Vereroudakis, E.; Masubuchi, Y.; Ianniruberto, G.; Marrucci, G.; Vlassopoulos, D. Undershoots in Shear Startup of Entangled Linear Polymer Blends. *J. Non-Newtonian Fluid Mech.* **2023**, *315*, No. 105028.

https://doi.org/10.1021/acs.macromol.5c00553
Macromolecules 2025, 58, 7062−7083